

## Structure and electronic properties of InN and In-rich group III-nitride alloys

This article has been downloaded from IOPscience. Please scroll down to see the full text article.

2006 J. Phys. D: Appl. Phys. 39 R83

(<http://iopscience.iop.org/0022-3727/39/5/R01>)

View [the table of contents for this issue](#), or go to the [journal homepage](#) for more

Download details:

IP Address: 152.14.136.96

The article was downloaded on 14/05/2013 at 09:18

Please note that [terms and conditions apply](#).

## TOPICAL REVIEW

# Structure and electronic properties of InN and In-rich group III-nitride alloys

W Walukiewicz<sup>1</sup>, J W Ager III<sup>1</sup>, K M Yu<sup>1</sup>, Z Liliental-Weber<sup>1</sup>,  
J Wu<sup>2</sup>, S X Li<sup>1,3</sup>, R E Jones<sup>1,3</sup> and J D Denlinger<sup>4</sup>

<sup>1</sup> Electronic Materials Program, Materials Sciences Division, Lawrence Berkeley National Laboratory, Berkeley, CA 94720, USA

<sup>2</sup> Department of Chemistry and Chemical Biology, Harvard University, Cambridge, MA 02138, USA

<sup>3</sup> Department of Materials Science and Engineering, University of California, Berkeley, CA 94720, USA

<sup>4</sup> Advanced Light Source Division, Lawrence Berkeley National Laboratory, Berkeley, CA 94720, USA

E-mail: [W\\_Walukiewicz@lbl.gov](mailto:W_Walukiewicz@lbl.gov)

Received 1 December 2005

Published 17 February 2006

Online at [stacks.iop.org/JPhysD/39/R83](http://stacks.iop.org/JPhysD/39/R83)

## Abstract

The experimental study of InN and In-rich InGaN by a number of structural, optical and electrical methods is reviewed. Recent advances in thin film growth have produced single crystal epitaxial layers of InN which are similar in structural quality to GaN films made under similar conditions and which can have electron concentrations below  $1 \times 10^{18} \text{ cm}^{-3}$  and mobilities exceeding  $2000 \text{ cm}^2 (\text{Vs})^{-1}$ . Optical absorption, photoluminescence, photo-modulated reflectance and soft x-ray spectroscopy measurements were used to establish that the room temperature band gap of InN is  $0.67 \pm 0.05 \text{ eV}$ . Experimental measurements of the electron effective mass in InN are presented and interpreted in terms of a non-parabolic conduction band caused by the  $k \cdot p$  interaction across the narrow gap. Energetic particle irradiation is shown to be an effective method to control the electron concentration,  $n$ , in undoped InN. Optical studies of irradiated InN reveal a large Burstein–Moss shift of the absorption edge with increasing  $n$ . Fundamental studies of the energy levels of defects in InN and of electron transport are also reviewed. Finally, the current experimental evidence for p-type activity in Mg-doped InN is evaluated.

(Some figures in this article are in colour only in the electronic version)

## 1. Introduction

In the last decade, the group III-nitrides—AlN, GaN, InN and their alloys—have become one of the most important classes of semiconductor materials. In particular, GaN and Ga-rich  $\text{In}_x\text{Ga}_{1-x}\text{N}$  and  $\text{Al}_x\text{Ga}_{1-x}\text{N}$  thin films are used in a variety of commercial optoelectronic devices, including green and blue light emitting diodes (LEDs) and lasers [1]. By combining UV-emitting GaN LEDs with phosphors it is

possible to fabricate high-efficiency white light emitters which are predicted to play a crucial role in future high-efficiency home and commercial lighting systems [2]. Group III-nitrides have also found applications in other electronic devices. For example, advanced GaN/AlGaN high-power microwave transistors are now commercially available.

The spectacular progress in developing applications of GaN and Ga-rich group III-nitride alloys was initially made possible by advances in materials synthesis and was guided

by a detailed understanding of the fundamental properties of these materials. Although AlN has been much less studied than GaN, its properties are also quite well established. At present, there are a number of established methods to grow GaN and AlN thin films, and both materials can be synthesized as bulk crystals.

In contrast to GaN and AlN, very little is known about InN. Until recently, synthesis difficulties prevented the preparation of good quality single crystals, leaving many of the key parameters of this material difficult to determine. For this reason, InN has been the least studied of the group III-nitrides. The first InN samples were prepared more than 30 years ago using radio-frequency sputtering of metallic In in a nitrogen atmosphere [3]. The samples were polycrystalline with electron concentrations in the high  $10^{18} \text{ cm}^{-3}$  range and a maximum electron mobility of about  $250 \text{ cm}^2 (\text{Vs})^{-1}$ . Later InN samples grown by similar methods by other groups showed electron mobilities of about  $100 \text{ cm}^2 (\text{Vs})^{-1}$  and higher electron concentrations well in excess of  $10^{19} \text{ cm}^{-3}$  [4, 5]. A notable exception was the work done by Foley and Tansley who reported electron mobilities as high as  $3980 \text{ cm}^2 (\text{Vs})^{-1}$  and electron concentrations in the mid- $10^{16} \text{ cm}^{-3}$  range [6]. It should be noted, however, that recent attempts to reproduce these results with the same growth equipment produced samples with electron concentrations of more than  $3 \times 10^{19} \text{ cm}^{-3}$  and mobilities of less than  $100 \text{ cm}^2 (\text{Vs})^{-1}$  [7]. These values are more comparable to results obtained for RF-sputtered polycrystalline films produced by other researchers [5]. The low concentration, high mobility samples synthesized by Foley and Tansley [8] showed a strong absorption edge at about 1.9 eV that was attributed to the fundamental energy gap of InN. This value of the band gap was widely accepted despite the fact that optical emission had not been reported at energies close to the claimed direct band gap energy.

In the early 1990s during the development of GaN-based devices, the band gap of  $\text{In}_x\text{Ga}_{1-x}\text{N}$  thin films with increasing values of  $x$  was investigated. One report found that the energy gap decreased very rapidly with increasing In content and fell well below 2 eV for  $x = 0.5$ , suggesting that the energy gap of InN is significantly less than 1.9 eV [9]. Other groups working with somewhat smaller values of  $x$  suggested that the low energy gaps in  $\text{In}_x\text{Ga}_{1-x}\text{N}$  could be explained by an unconventionally large bowing parameter [10].

A major breakthrough in InN research occurred a few years ago when good quality single crystal films were grown by molecular beam epitaxy (MBE) on sapphire substrates [11–14]. There has been consistent improvement of the electrical properties of MBE-grown InN; typical electron concentrations have been reduced into low  $10^{18} \text{ cm}^{-3}$  range with room temperature electron mobilities in excess of  $1000 \text{ cm}^2 (\text{Vs})^{-1}$ . At present, the highest reported electron mobility of about  $2200 \text{ cm}^2 (\text{Vs})^{-1}$  was found in a sample with an electron concentration of  $3 \times 10^{17} \text{ cm}^{-3}$  [15].

The availability of high-quality single crystals has created the opportunity for the systematic investigation of the fundamental properties of InN. Most significantly, optical absorption, photoluminescence (PL), and photomodulated reflection (PR) measured on MBE-grown InN with low electron concentrations have shown that the energy gap of

InN is  $0.67 \pm 0.05 \text{ eV}$  [12, 16, 17], about 1/3 the previously accepted value. The low energy gap has found support in band structure calculations performed by two different groups [18, 19]. It should be noted that these reports have generated some controversy. There are claims that the low energy transitions observed in the above-referenced optical measurements originate from deep levels associated with point defects related to non-stoichiometry [20, 21].

The potential of extending the band gap energies of the group III-nitrides into the near infrared spectral region has generated considerable interest, and extensive research efforts have been initiated by research groups worldwide. The low band gap results have been reproduced by several groups using films grown by MBE and metalorganic chemical vapour deposition (MOCVD) and employing various material characterization methods. The results of this extensive research have been reported in hundreds of papers, and there have been a number of specialized workshops and reviews addressing different aspects of the research on InN and In-rich group III-nitride alloys [17, 22–26].

In this paper we review the current status of research on InN and In-rich group III-nitride alloys. We show that the combination of various experimental techniques and theoretical modelling provides the basis for a good understanding of the energy band structure of these materials. With very few exceptions, most reported experimental data concerning the optical and electrical properties of InN are consistent with a low energy gap. Observed variations in the properties of InN samples can be attributed to unique features of the electronic band structure and their effect on the nature and abundance of native defects.

In section 2 we discuss the challenges involved in the thin film growth of InN and In-rich InGa<sub>1-x</sub>N, with an emphasis on obtaining single-phase materials suitable for detailed optical and electronic study. In section 3, we review the combined optical spectroscopy and theoretical analysis that has established the band gap energy of InN and determined important aspects of the conduction band structure. In section 4, we review the electrical properties of InN, with an emphasis on the relationship between electron concentration and mobility. We also discuss at the end of section 4 an outstanding challenge in InN technology, namely the synthesis of p-type material.

## 2. Thin film growth and structural characterization

### 2.1. Film growth

As discussed above, InN was the last of the III-nitrides to be synthesized in high-quality form by MBE. Recently, InN has been grown with MOCVD; Bhuiyan *et al* [27] have reviewed this experimental literature. Growth of InGa<sub>1-x</sub>N alloys has been predicted to be difficult. Due to the large difference in lattice constants between GaN and InN, a large miscibility gap is expected [28–30]. Specifically, the critical temperature for growth of  $\text{In}_{0.5}\text{Ga}_{0.5}\text{N}$  is predicted to be  $1250^\circ\text{C}$ ; this exceeds the melting point of InN [28]. Also, due to the large vapour pressure of  $\text{N}_2$  over InN, growth of InN and In-rich InGa<sub>1-x</sub>N is constrained to much lower temperatures, in the  $500\text{--}750^\circ\text{C}$  range [27]. A number of groups have attempted growth

of  $\text{In}_x\text{Ga}_{1-x}\text{N}$  with  $x > 0.2$ ; except for the case of very thin ( $< 50\text{ nm}$ ) quantum wells in GaN, both MBE [31] and MOCVD [32–34] deposition efforts prior to 2000 reported phase-separated and/or low structural quality films. Most recently, MBE growth of single-phase  $\text{In}_x\text{Ga}_{1-x}\text{N}$  alloys with  $0.37 < x < 1.0$  [35] and with  $0.06 < x < 0.97$  has been reported [36].

## 2.2. Structural characterization: electron microscopy, x-ray diffraction and Rutherford backscattering spectrometry

Given the challenges in growing InN and In-rich  $\text{In}_x\text{Ga}_{1-x}\text{N}$  discussed above, a detailed structural characterization is required to establish that the films are of sufficient quality in order to perform meaningful and reliable measurements of the properties of these materials [37]. An approach that has proved to be successful is described below. X-ray diffraction (XRD) in the  $\theta$ – $2\theta$  coupled geometry using  $\text{Cu K}\alpha$  x-rays is used to evaluate the presence of secondary phases, polycrystallinity and, in the case of alloy films, phase separation and related effects. The microstructure of InN and InGaN films is typically investigated in detail by transmission electron microscopy (TEM) in cross-section and plan-view configurations. We note that care must be taken in the sample preparation and examination to avoid conditions that would decompose the InN/InGaN and potentially form metallic In. Finally, Rutherford backscattering spectrometry (RBS) measurements are used to assess film stoichiometry.

Figure 1(a) shows the XRD pattern of a typical optimized MBE-grown InN film in which only the (0001) diffraction peaks of wurzite InN, GaN (buffer layer) AlN (nucleation layer) and sapphire (substrate) are observed. The inset in this figure shows a high resolution scan in the region of the InN 0002 diffraction ( $30^\circ < 2\theta < 37^\circ$ ). RBS spectra from the same InN film shown in (a) taken in both random and (0001) aligned channelling directions are shown in figure 1(b). The minimum yield  $\chi_{\min}$  (ratio of the channelled yields with the random yields) of this InN is  $< 0.04$  with a very small increase in the dechannelling slope over a film thickness of  $> 1\ \mu\text{m}$ . This indicates that the InN is of high crystalline quality with a relatively low density of extended defects.

The high structural quality of this InN film is further confirmed by the transmission electron micrograph shown in figure 1(c). We find that for films grown under optimized MBE growth conditions the measured dislocation densities do not exceed  $\text{mid-}10^{10}\text{ cm}^{-2}$ . By comparison, high quality GaN films grown on sapphire by MBE typically have  $10^9$  dislocations  $\text{cm}^{-2}$ . Most of the dislocations are of edge character. Selected area electron diffraction (SAD) patterns (shown in the inset of figure 1(c)) consist of a single wurzite InN diffraction pattern with no additional spots which could suggest the existence of secondary phases or metallic In.

The interpretation of optical absorption and PL data from InN has been questioned recently by Shubina *et al* [20]. It has been claimed that the absorption edge of InN at 0.7 eV actually results from resonant Mie scattering by metallic indium clusters and that PL at  $\sim 0.7\text{ eV}$  in InN originates from optical transitions involving interface states between the In clusters and the InN matrix. These authors assigned an

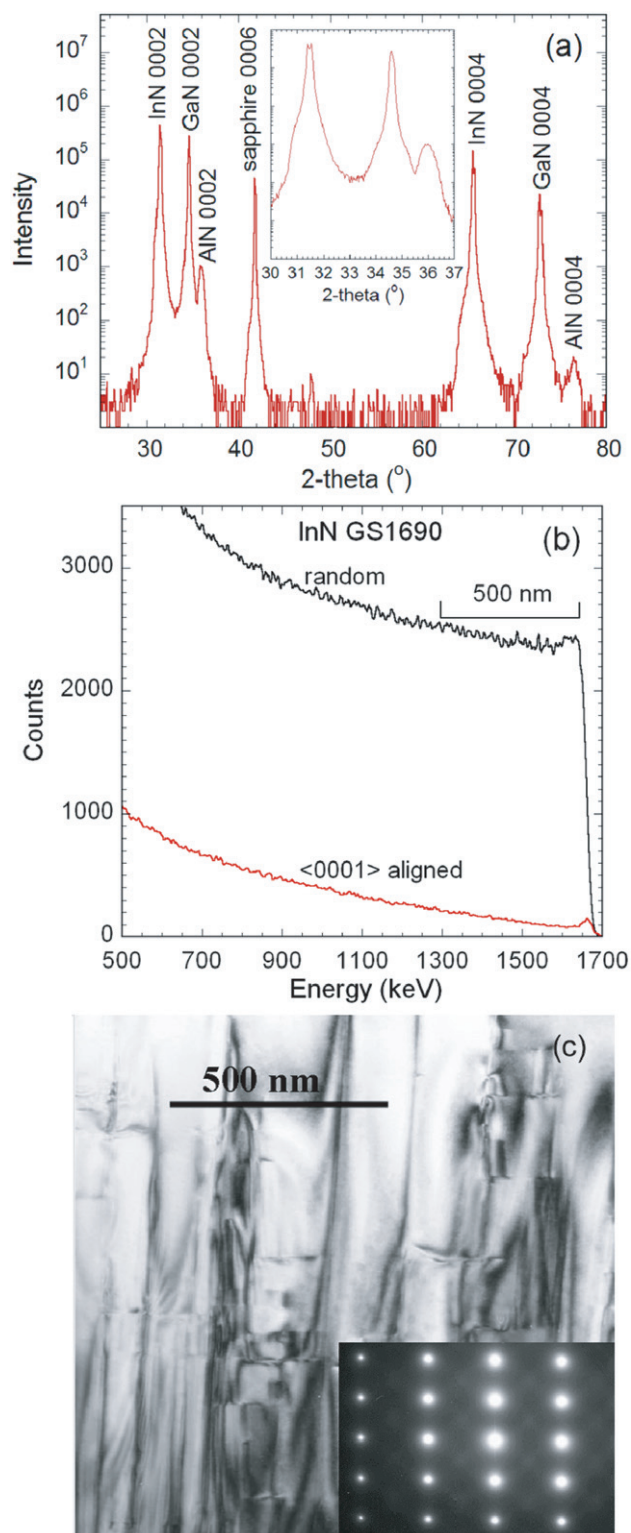


**Figure 1.** X-ray diffraction patterns from (a) a high-quality InN film grown by MBE on GaN/AlN buffer layer on sapphire. The inset shows a high resolution scan in the region of the 0002 diffraction ( $2\theta$  of  $30^\circ$ – $37^\circ$ ). (b) RBS spectra from the same InN film shown in (a) taken in both random and (0001) aligned channelling direction. (c) Cross-section TEM micrograph of an MBE-grown InN film. The inset shows the monocrystalline diffraction pattern of InN with a 1010 zone axis.



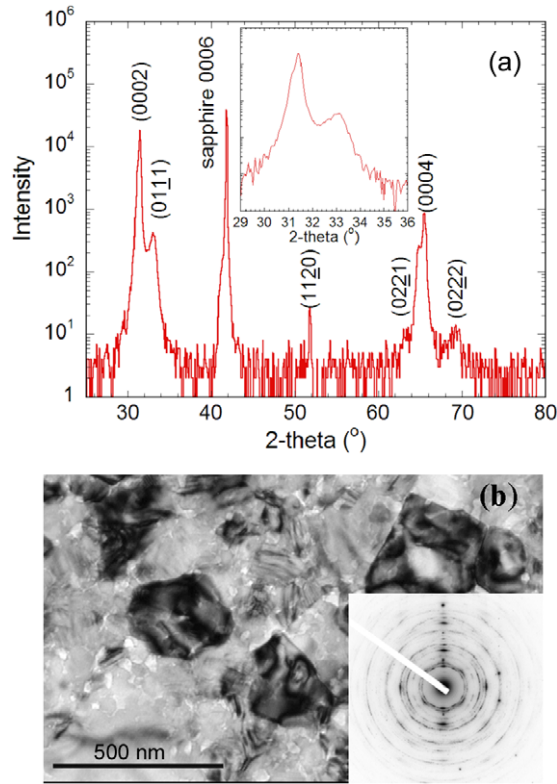


**Figure 2.** (a) XRD pattern from a low-quality InN film grown directly on sapphire (GS1489). The assignment of all observed features to InN is shown. A high resolution scan around the  $33^\circ$  peak is shown in the inset. (b) Plan-view TEM micrograph of this polycrystalline InN film; the inset shows the characteristic ring pattern of the SAD data. No evidence of metallic In is found in this film.

‘anomalous’ peak from XRD spectra at  $2\theta \sim 33^\circ$  to metallic In (we note that no peak at  $33^\circ$  appears in the XRD pattern shown in figure 1). To elucidate the origin of the ‘anomalous’  $33^\circ$  XRD peak we have investigated an InN film grown directly on sapphire without the AlN nucleation layer and the GaN buffer layer. As a result of these non-optimal MBE growth conditions, this InN film is expected to be of poor crystalline quality. The XRD pattern shown in figure 2(a) shows that in addition to the  $33^\circ$  peak, diffraction peaks at  $\approx 52^\circ$  ( $d = 1.76 \text{ \AA}$ ),  $63^\circ$  ( $d = 1.48 \text{ \AA}$ ) and  $69^\circ$  ( $d = 1.36 \text{ \AA}$ ) are also present. These, and the  $33^\circ$  peak, can all be assigned to diffraction peaks of randomly oriented InN grains. Additional evidence for the absence of metallic In in this film was obtained by TEM. A TEM image and electron diffraction pattern from this film are shown in figure 2(b). The micrograph and the ring pattern in the SAD (inset) clearly reveal that the film is polycrystalline in nature. Using the sapphire substrate as an internal standard to precisely determine the camera length, all consecutive diffraction rings in the SAD pattern could be assigned to InN. The interplanar distances  $d$  obtained from the SAD and XRD are in excellent agreement with calculated values for wurzite InN.

We assign the  $33^\circ$  peak in figure 2(a) to the  $(10\bar{1}1)$  reflection of polycrystalline InN. We note that the InN  $d_{(10\bar{1}1)}$  of  $2.69 \text{ \AA}$  is very close to the  $d_{101}$  of metallic In ( $2.72 \text{ \AA}$ ). Both these  $d$  spacings would give rise to a diffraction peak at

$33^\circ$  in XRD. However, none of the other interplanar distances which would be expected from In such as 002 ( $2.47 \text{ \AA}$ ), 110 ( $2.3 \text{ \AA}$ ) or 112 ( $1.68 \text{ \AA}$ ) are observed in either the SAD or XRD patterns. Some larger grains were studied individually by SAD and patterns consistent with InN in different orientations were observed. The RBS, XRD and TEM results from the InN film GS1489 grown directly on sapphire show that the film is polycrystalline and stoichiometric. In this film, the ‘anomalous’  $33^\circ$  peak is in fact the  $(01\bar{1}1)$  diffraction peak of InN. No evidence of metallic In is observed. Thus we consider it likely that the  $33^\circ$  XRD line observed in some InN films and assigned to In in the literature [20] is due to polycrystalline InN and not to metallic In.

### 2.3. Phase separation and compositional modulation in $\text{In}_x\text{Ga}_{1-x}\text{N}$

As discussed in section 2.1, phase separation is an additional consideration in  $\text{In}_x\text{Ga}_{1-x}\text{N}$ , particularly at compositions near  $x = 0.5$ . Optimized MBE growth conditions can produce single-phase films. Figure 3 shows XRD and TEM data from a single-phase  $\text{In}_{0.37}\text{Ga}_{0.63}\text{N}$  film grown on a GaN buffer layer [35]. The dislocation density is about  $2 \times 10^{10} \text{ cm}^{-2}$ , similar to InN films grown by MBE, and edge dislocations are the most prevalent. Interestingly, in the TEM micrograph shown in figure 3(b) it appears that some dislocations in the GaN buffer layer do not propagate into the InGaN layer. In cases when the growth conditions are not optimized, phase separation can occur. This can be observed easily in XRD. Figure 4 shows the XRD pattern from a film grown by MOCVD with a target composition of  $x = 0.44$ . Phase separation into InN,  $\text{In}_{0.68}\text{Ga}_{0.32}\text{N}$  and  $\text{In}_{0.43}\text{Ga}_{0.57}\text{N}$  is seen clearly.

Finally, we note that under certain growth conditions, periodic compositional modulation with an average orientation along the  $c$ -axis has been observed by TEM and/or XRD for MBE-grown  $\text{In}_x\text{Ga}_{1-x}\text{N}$  films with  $0.45 < x < 0.78$  [35, 38]. The modulation period as measured by XRD is between 2 and 6 nm and increases with increasing lattice mismatch with the buffer layer (AlN or GaN). As shown in figure 5, the modulation produces clear superlattice-like fringes in the XRD pattern. As shown by cross-sectional TEM in figure 6, the composition modulation leads to a parallel fringe pattern with light and dark contrast forming a shallow ‘w’ profile, which is observed in two perpendicular zone axes,  $[1100]$  and  $[11\bar{2}0]$ . High resolution Z-contrast imaging and energy-dispersive x-ray spectroscopy analysis along the fringe pattern were used to show that the amplitude of the composition modulation is ca 10 at%. The mechanistic origin of the modulation is not known at present, but time-varying fluxes of In and Ga during MBE growth and/or the tendency for In to segregate on certain crystallographic planes (known from GaN) are considered to be possibilities.

## 3. Electronic structure of InN: theory and experiments

### 3.1. Measurement of the InN bandgap with optical and x-ray techniques

As an example of the optical properties of typical wurzite InN films grown by MBE (figure 7) shows the PL and optical

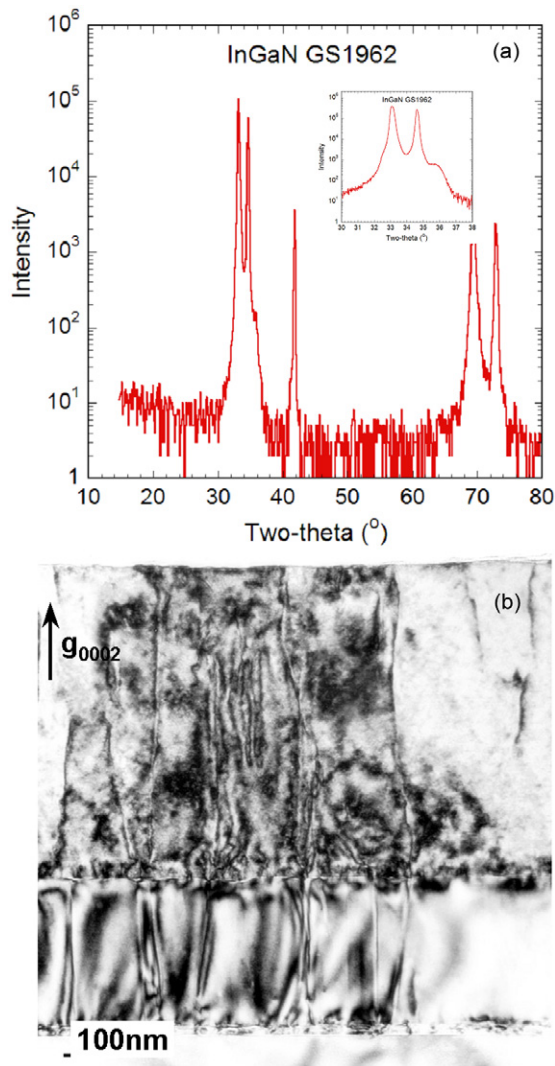


**Figure 3.** XRD (a) and TEM (b) analysis of a single phase  $\text{In}_{0.37}\text{Ga}_{0.63}\text{N}$  film grown by MBE on a GaN buffer layer on sapphire. No evidence of phase separation is observed.

absorption spectra recorded at 15 K [39]. This InN film (thickness =  $7.5\ \mu\text{m}$ ) was grown on (0001) sapphire with a GaN buffer layer ( $\sim 240\ \text{nm}$ ). This film was not intentionally doped and had a low free electron concentration of  $3.5 \times 10^{17}\ \text{cm}^{-3}$  and a high carrier mobility of  $2050\ \text{cm}^2\ (\text{Vs})^{-1}$  measured by the Hall effect [39]. The optical absorption curve shows an onset at  $\sim 0.68\ \text{eV}$ , while the PL peak is located at  $0.67\ \text{eV}$ . There is no noticeable band gap feature in the  $1.8\text{--}2.0\ \text{eV}$  region (not shown), i.e. in the energy range of previously reported band gaps. The simultaneous observations of the absorption edge and the PL at essentially the same energy indicate that this energy position corresponds to the transition across the fundamental band gap of InN. Optical absorption and PL data for a series of  $\text{In}_x\text{Ga}_{1-x}\text{N}$  films with  $0.37 < x < 1.0$  are shown in figure 8; the absorption edge and the PL emission peak are in excellent correspondence, indicating that the direct gap of InGaN is being measured.

The temperature behaviour of the intrinsic InN bandgap has also been measured by performing optical absorption on a high-purity film at temperatures ranging from room

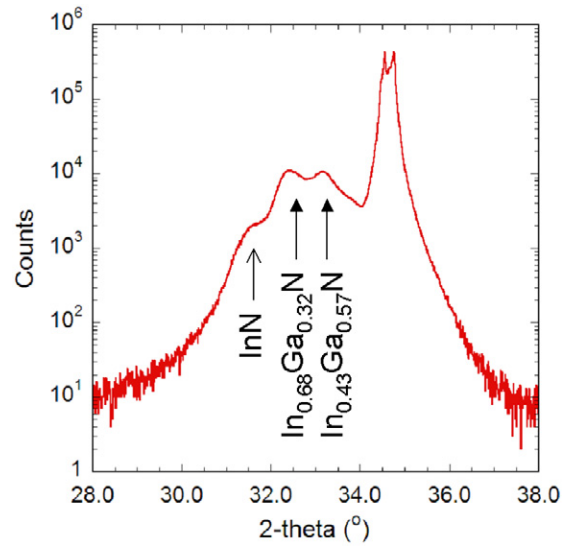


**Figure 4.** XRD pattern obtained from MOCVD grown InGaN films with a nominal composition of  $\text{In}_{0.44}\text{Ga}_{0.56}\text{N}$ . Phase separation is clearly seen in XRD. The strong peak at  $34.5^\circ$  is due to the GaN buffer layer.

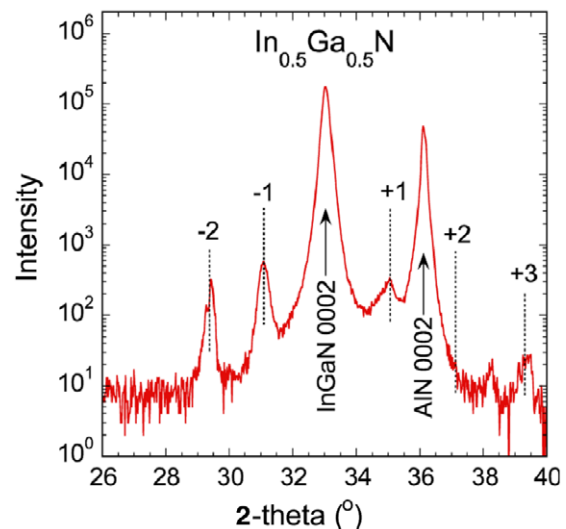


**Figure 5.** X-ray diffraction patterns ( $\theta$ – $2\theta$ ) for a  $230\ \text{nm}\ \text{In}_{0.5}\text{Ga}_{0.5}\text{N}$  film grown by MBE on a  $200\ \text{nm}\ \text{AlN}$  buffer; indicated superlattice peaks corresponding to a period of  $4.7\ \text{nm}$  are clearly observed.

temperature to 12 K [40]. The gap energy is plotted in figure 9 as a function of temperature along with the PL peak energies. As the temperature increases from 12 K to room temperature, the absorption edge shifts to lower energy by about  $47\ \text{meV}$ . The red shift is substantially weaker than in other group III-nitrides; hence the InN band gap has the weakest temperature dependence. The temperature dependence of a direct bandgap is usually described by Varshni's equation:

$$E_g(T) = E_g(0) - \frac{\gamma T^2}{T + \beta}. \quad (3.1)$$

The best fit of InN bandgap with equation (3.1) is obtained with  $E_g(0) = 0.69\ \text{eV}$ ,  $\gamma = 0.41\ \text{meV K}^{-1}$  and  $\beta = 454\ \text{K}$ .

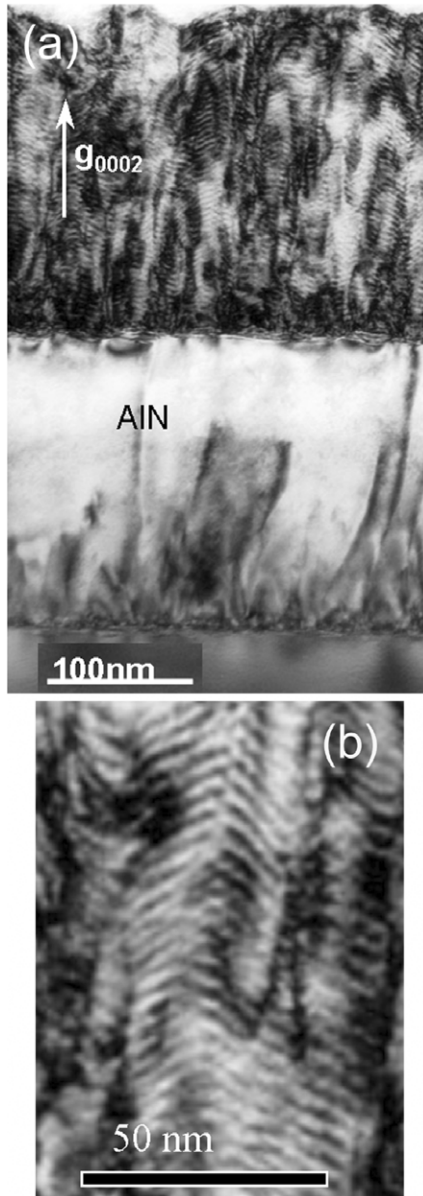


**Figure 6.** (a) TEM micrograph observed along the  $[\bar{1}1\bar{2}0]$  zone axis of a 230 nm  $\text{In}_{0.5}\text{Ga}_{0.5}\text{N}$  film grown by MBE on a 200 nm AlN buffer. The observed w-shaped fringe contrast is attributed to compositional modulation. Vertical lines are due to threading dislocations in both the AlN buffer layer and in the InGa layer. (b) Details of (a) showing the dark/light fringe contrast.

Nitrogen K-edge soft x-ray absorption (XAS) and emission (SXE) using linearly-polarized synchrotron radiation were performed in order to separately monitor the changes in the conduction and valence partial density of states. XAS measures the energy difference between the N 1s core level and the unoccupied conduction band. SXE measures the difference between the occupied valence band and the N 1s core hole. Total fluorescence yield detection was used so as to be sensitive to the bulk ( $\sim 100$  nm) of the InN films rather than to the near surface area (where electron accumulation is expected, section 4). By overlaying XAS and SXE measurements, the bandgap of InN can be evaluated, as shown in figure 10 [41].

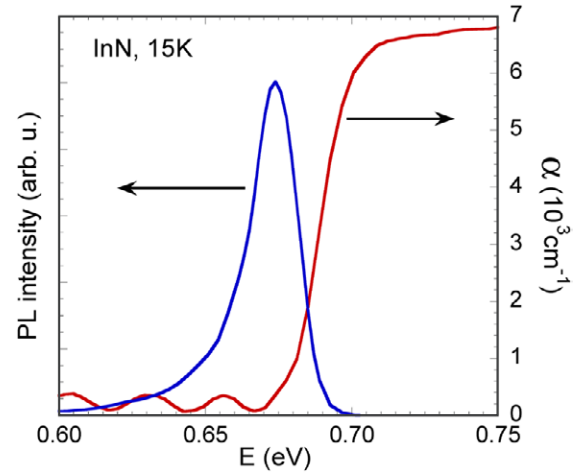


**Figure 7.** Photoluminescence and absorption spectra of a typical, undoped InN film grown by MBE [39]. The oscillation of the absorption curve below the absorption edge is caused by the Fabry–Perrot interference.

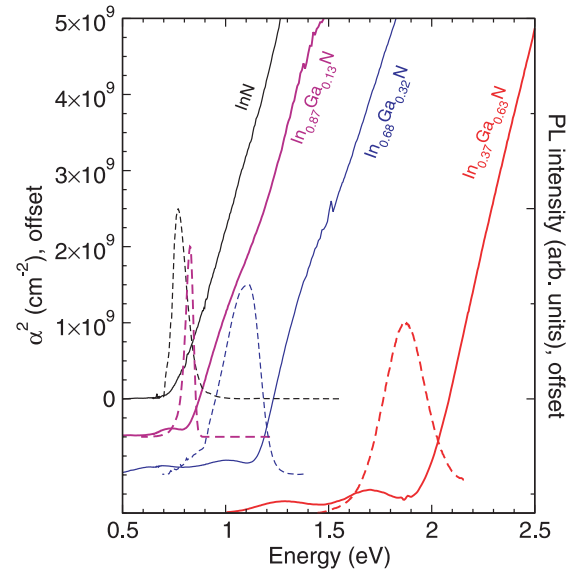


**Figure 8.** Photoluminescence (dotted lines) and absorption (solid lines) spectra for a series of  $\text{In}_x\text{Ga}_{1-x}\text{N}$  films. The peak of the PL emission corresponds with the optical absorption edge.

The x-ray data are consistent with a band gap of 0.7 eV, in agreement with optical measurements.

Combining the optical measurements on InN and In-rich  $\text{In}_x\text{Ga}_{1-x}\text{N}$  discussed above with previous reports for Ga-rich InGaN, AlGaIn and AlInN [42] allows a complete picture of the band gap bowing in the III-nitrides to be developed. The direct band gaps in this alloy system are displayed in figure 11 as a function of lattice parameter. Calculated bowing parameters are 1.4 eV for InGaIn, 3.0 eV for AlInN and 1.4 eV for AlGaIn. Interestingly, the bowing parameters scale nearly exactly with the band gap difference between the end point compounds.

### 3.2. Band structure theory

This narrow gap of InN is not only much smaller than the previously believed value of  $\sim 1.9$  eV, but also lower than



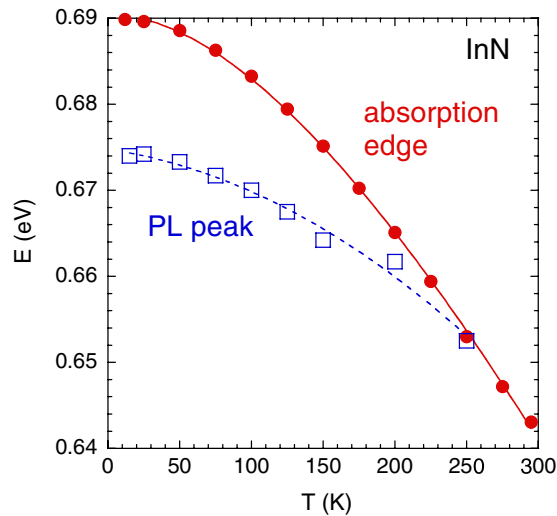


**Figure 9.** Temperature dependence of the intrinsic bandgap of InN by measuring the absorption edge of an undoped InN film [39]. The PL peak energy is also shown as a comparison. The solid line is a fit using equation (3.1), and the dashed line is a guide to the eye.

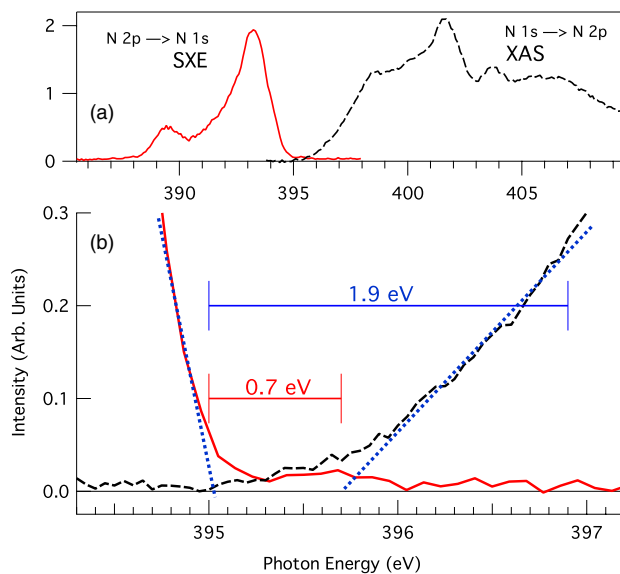


**Figure 10.** Soft x-ray absorption spectroscopy (XAS) and soft x-ray emission (SXE) measurements from an InN film with an electron concentration of  $1 \times 10^{18} \text{ cm}^{-3}$  and a mobility of  $1560 \text{ cm}^2 (\text{Vs})^{-1}$  [41]. XAS measures the transition from the N 1s core level to the unoccupied conduction band and SXE measures the transition from the occupied valence band to the N 1s core hole. (a) Overlay of SXE (solid) and XAS (dashed) spectra obtained with an energy resolution of 0.1 eV. (b) Detail of (a), showing fitting of the absorption and emission edges to estimate the band gap. The data are consistent with a band gap for InN of 0.7 eV.

the bandgap of InP (1.4 eV), which could be considered counter-intuitive because the bandgap is expected to increase as the anion atomic number decreases in common-cation semiconductors. It should be noted, however, that similar behaviour has been observed in other semiconductor systems. For example, the energy gap of ZnO (3.4 eV) is smaller than the energy gap of ZnS (3.7 eV) and the energy gap of CdO is slightly smaller than the energy gap of CdS [22].

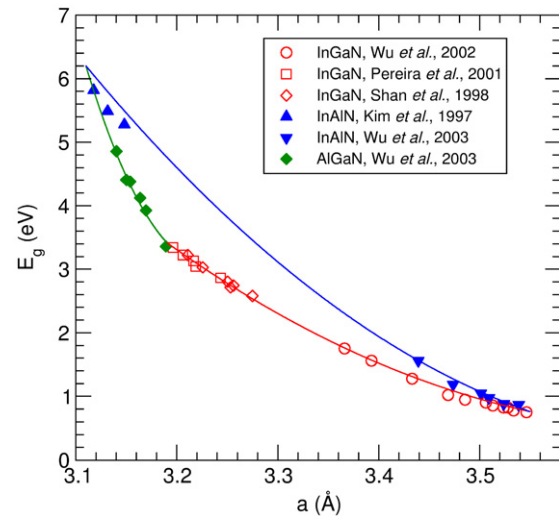


**Figure 11.** Measured band gap values for all alloys in the III-nitride alloy system, adapted from [42]. Lines are fits to the standard bowing parameter equation, as discussed in the text.

Following the discovery of the low energy gap, several theoretical groups have attempted to calculate the energy gap of InN. Bechstedt *et al* used density functional theory (DFT) within the local density approximation (LDA) to calculate energy gap of the wurtzite and cubic phases of InN [18]. These calculations gave negative values for the band gaps. However, by incorporating self-interaction and quasiparticle corrections, positive gap values of 0.6 eV (0.8 eV) were obtained for the cubic (wurtzite) phases. Carrier and Wei [19,43] performed LDA band structure calculation with semi-empirical corrections to illuminate the apparent exception to the common-cation rule discussed above. First, since the conduction band minimum at the  $\Gamma$  point is an anion s and a cation s state, the much lower 2s atomic orbital energy of N (−18.49 eV), compared with P (−14.09 eV), lowers the conduction band minimum. Second, the smaller bandgap deformation potential of InN (−3.7 eV), as compared with InP (−5.9 eV), weakens the atomic size effect that would normally increase the bandgap of semiconductors consisting of smaller atoms.

The narrow bandgap is expected to result in a strong  $\mathbf{k} \cdot \mathbf{p}$  interaction between the conduction band and the valence bands and consequently a strongly non-parabolic conduction band with a wavevector-dependent effective electron mass. The non-parabolicity of the conduction band in narrow gap semiconductors, such as InSb [44] and InAs [45], has been well studied. Neglecting the spin-orbit and crystal-field splittings in InN, an analytical form of the conduction band dispersion is obtained following Kane's  $\mathbf{k} \cdot \mathbf{p}$  perturbation approach [44],

$$E_C(\mathbf{k}) = E_g + \frac{\hbar^2 k^2}{2m_0} + \frac{1}{2} \left( \sqrt{E_g^2 + 4E_P \cdot \frac{\hbar^2 k^2}{2m_0}} - E_g \right), \quad (3.2)$$

where  $E_g$  is the intrinsic bandgap energy and  $E_P = 2|\langle S|P_x|X \rangle|^2/m_0$  is an energy parameter related to the interaction momentum matrix element [44]. In this model the perturbation from remote conduction bands is neglected, since other conduction bands are at least 2.3 eV ( $>3E_g$ ) away (A-valley) [19].



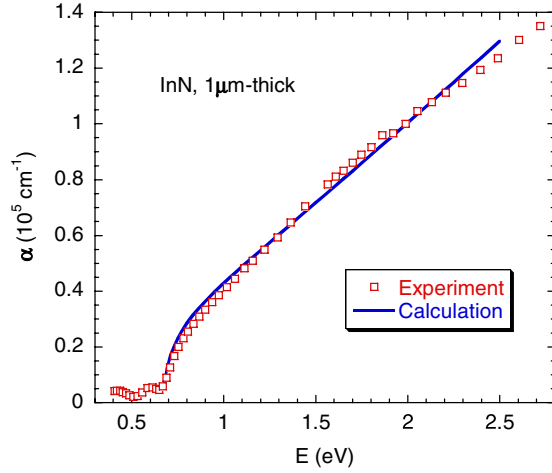


**Figure 12.** Optical absorption spectrum of InN plotted together with the calculation from equation (3.3).

In addition to the modification of the dispersion relation, the  $\mathbf{k} \cdot \mathbf{p}$  interaction mixes the conduction and the valence band states which affects the symmetry of the wavefunctions and thus also the dipole matrix elements for interband optical transitions. The interband optical absorption can be calculated using the expression [44]:

$$\alpha(E) = \frac{4\pi^2 q^2 \hbar}{m_0^2 c n E} \sum_j M_j^2 \rho_j(E), \quad (3.3)$$

where  $M_j$  is the optical matrix element averaged over direction and summed over degenerate bands and  $\rho_j$  is the joint density of states. The summation index,  $j$ , refers to the three valence bands: heavy hole, light hole and split-off. The effects of the  $\mathbf{k} \cdot \mathbf{p}$  interaction are incorporated through the modified density of states and the dipole matrix elements for the non-parabolic bands. Figure 12 shows the absorption spectra calculated from (3.2) and (3.3) using  $E_p = 10$  eV and an energy gap of 0.68 eV (solid line) together with experiment data (squares) over a broad photon energy range; theory and experiment are in excellent quantitative agreement. It is worth noting that there is no discernible change in the absorption coefficient at 1.9 eV, which is the energy of the previously accepted band gap of InN.

Using the standard definition, the electron effective mass can be calculated from the following equation:

$$m^*(k) = \frac{\hbar^2 k}{dE_C(k)/dk}, \quad (3.4)$$

where the dispersion  $E_C(k)$  is given by equation (3.2). The effective mass of the conduction band electrons can be evaluated experimentally from the plasma reflection in the far infrared region [46]. The plasma frequency,  $\omega_p$ , determined from the reflection spectra, is given by the following equation:

$$\omega_p = \sqrt{\frac{ne^2}{\epsilon_0 \epsilon_\infty m^*}}, \quad (3.5)$$

where  $n$  is the electron concentration and  $\epsilon_\infty = 6.7$  is the optical dielectric constant of InN [47]. The experimental

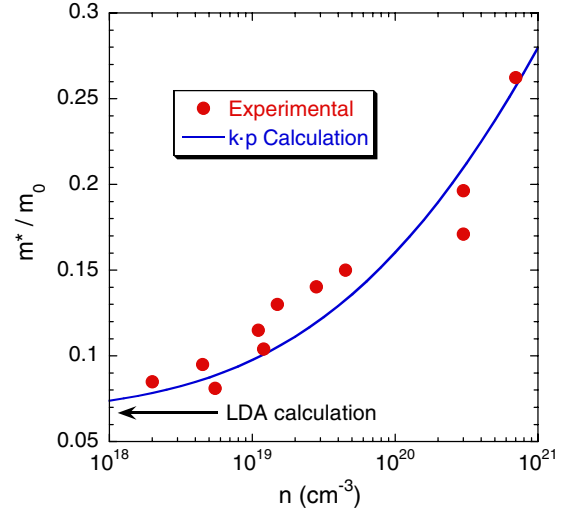


**Figure 13.** Electron effective mass of InN as a function of the free electron concentration [48]. The theoretical curve is based on Kane's model using  $E_p = 10$  eV. A LDA-calculated, isotropically-averaged  $m^*$  at the conduction band minimum is indicated by the arrow [19].

electron effective mass obtained from measurements on InN films with  $2 \times 10^{18} < n < 7 \times 10^{20} \text{ cm}^{-3}$  is plotted as a function of  $n$  in figure 13 [48]. The effective mass increases by over a factor of three over this range of  $n$ .

The observed strong dependence of the electron effective mass upon carrier concentration confirms that the conduction band of InN is highly non-parabolic. The solid line in figure 13 represents the effective mass calculated using equations (3.2) and (3.4) with  $E_g = 0.7$  eV and  $E_p = 10$  eV. The calculations agree well with the experimental results from samples grown with a number of different techniques. The calculated effective mass curve can be extrapolated to an effective mass of  $0.07m_0$  in intrinsic InN. This value is also consistent with a recent LDA calculation which yields an isotropically-averaged  $m^* = 0.066m_0$  at the conduction band minimum [19].

### 3.3. Burstein–Moss shift in InN observed in optical absorption

The small electron effective mass, and thus also the conduction band density of states, has important consequences for the effects of n-type doping on the absorption edge energy. It has been shown that the wide range of reported bandgap values of InN can be attributed to conduction band filling as the free electron concentration increases, an effect known as the Burstein–Moss shift [48, 49]. At degenerate doping levels, where the conduction band is filled with a large number of electrons, optical absorption occurs only for photons with energy higher than the threshold energy needed for electrons to make vertical, momentum conserving, transitions from the valence band up to the Fermi surface in the conduction band, as shown in the inset of figure 14. The Fermi energy is given by the conduction band dispersion in equation (3.2) evaluated at the Fermi wavevector  $k_F = (3\pi^2 n)^{1/3}$ . In addition, at high doping levels the value of the energy gap and thus also the Burstein–Moss shift is affected by the band gap renormalization effects. The band gap is reduced by electron–ion and electron–electron interactions [47]. Figure 14 shows

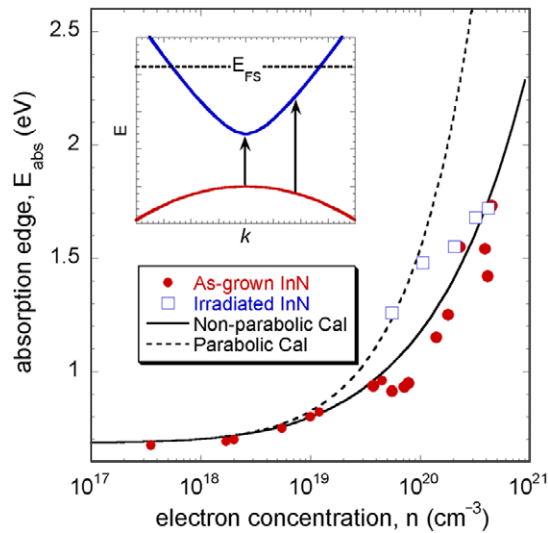


**Figure 14.** Optical absorption edge as a function of the free electron concentration for as-grown InN [49] and for irradiated InN (section 4.2). The curves show the calculation based on the Burstein-Moss shift, including or excluding the conduction band non-parabolicity [49]. The inset schematically shows the increase of the optical absorption threshold energy as free electrons fill the conduction band. As discussed in section 4.4, the Burstein-Moss shift saturates when  $E_F$  reaches the Fermi stabilization energy,  $E_{FS}$ .

the comparison between the experimental absorption edge (referred to as the optical bandgap) and the calculation based on the Burstein-Moss effect. Data from irradiated InN, in which the concentration of electrons was varied by intentional crystal lattice damage (see section 4.2), are also included. The solid line that represents calculations of the Burstein-Moss shift of the absorption edge, in which both the non-parabolicity and the band gap renormalization effects are properly taken into account, is in a good agreement with the experiment. As is shown by the dashed curve, the calculation that neglects these effects does not agree with the experimental results, particularly at high values of  $n$ . It is seen in figure 14 that the optical bandgap increases from  $\sim 0.7$  eV, the intrinsic bandgap of InN, to  $\sim 2$  eV for  $n \sim 6 \times 10^{20} \text{ cm}^{-3}$ . The  $\sim 2$  eV absorption edge previously observed in sputter-grown, degenerately-doped InN films thus over-estimates the intrinsic bandgap of InN.

The frequency-dependent dielectric function of InN has also been measured from the mid-infrared to the ultraviolet range employing spectroscopic ellipsometry [26, 50]. Five critical points (CPs) were identified from the differentiation curves of the dielectric functions. The CP,  $E_0$ , corresponding to the direct bandgap,  $E_g$ , in optical absorption measurements was determined to be  $\sim 0.65$  eV and found to increase as the electron concentration increases, consistent with the optical absorption measurements discussed above. The strongest of these CP structures (5.41 eV) was assigned to the interband transition at the  $L$  point of the Brillouin zone. The other three CPs were in correspondence with other interband transitions derived from pseudopotential calculations. Unlike  $E_0$ , these high-energy CPs do not exhibit strong dependence on the electron concentration, which is consistent with the fact that only the bottom of the conduction band is affected by the free electron doping.

## 4. Doping properties of InN

### 4.1. Native defects and electron concentration

It was realized very early that InN exhibits an exceptional tendency for n-type conductivity. As-grown samples are always n-type with electron concentrations in single-crystal wurtzite films ranging from mid- $10^{17}$  to  $10^{21} \text{ cm}^{-3}$ . As mentioned above, the lowest reported electron concentration to date for single crystal InN is  $3.15 \times 10^{17} \text{ cm}^{-3}$ , in a film with an electron mobility of  $2160 \text{ cm}^2 (\text{Vs})^{-1}$  [51]. The extreme propensity of InN for n-type doping can be traced to the extraordinarily low location of the conduction band edge in this material. The electron affinity of InN, 5.8 eV, is larger than that of any other known semiconductor.

Although impurity atoms, particularly H and O, were initially suggested to be the source of the innate n-type conductivity in InN, SIMS results have shown that their concentrations cannot always account for the high electron concentrations [49]. Instead the tendency for n-type conductivity can be explained by the amphoteric defect model (ADM) [40, 52, 53]. According to the ADM, formation energy of native defects depends on the location of the Fermi energy ( $E_F$ ) with respect to the common energy reference, the Fermi stabilization energy ( $E_{FS}$ ).  $E_{FS}$  can equivalently be described as the average energy level of native defects. When  $E_F < E_{FS}$  ( $E_F > E_{FS}$ ), the formation energy of donor defects is reduced (increased) and that of acceptor defects is increased (reduced). This causes the preferential formation of donor (acceptor) defects, which then pushes  $E_F$  closer to  $E_{FS}$ . When  $E_F$  reaches  $E_{FS}$ , it is pinned there by the creation of donor and acceptor defects at equal rates. In most semiconductors  $E_{FS}$  is located in the band gap, and incorporation of native defects produces high resistivity material. In contrast, in InN  $E_{FS}$  is located extremely high in the conduction band, 0.9 eV above the conduction band edge [40, 54]. Therefore, for electron concentrations lower than mid- $10^{20} \text{ cm}^{-3}$ , the Fermi energy is located below  $E_{FS}$  and donor-like defects are preferentially formed. This provides the interesting possibility of controlling electron concentration by incorporation of native defects, which is discussed in the next section.

### 4.2. Control of electron concentration with energetic particle irradiation

To investigate the relationship between electrical properties and native defects, we have intentionally introduced native point defects into InN and  $\text{In}_x\text{Ga}_{1-x}\text{N}$  samples by irradiation with 1 MeV electrons, 2 MeV  $\text{H}^+$  and 2 MeV  $^4\text{He}^+$  particles. At the energies used, the particles penetrate through the InN and InGaN films and have a vacancy production rate that is approximately constant with depth. TEM (figure 15) and ion channelling spectroscopy have shown that irradiation produces point defects only and the samples remain single-crystal with no additional extended defects formed. The damage caused by the particles was quantified by the displacement damage dose methodology [55, 56]. The proportionality constant that relates the particle dose to the displacement damage dose,  $D_d$ , for InN is equal to  $2.9 \times 10^{-5} \text{ MeV cm}^2 \text{ g}^{-1}$  for 1 MeV electrons,  $0.0445 \text{ MeV cm}^2 \text{ g}^{-1}$  for 2 MeV protons and  $0.615 \text{ MeV cm}^2 \text{ g}^{-1}$  for 2 MeV  $\text{He}^+$  ions. For consistency

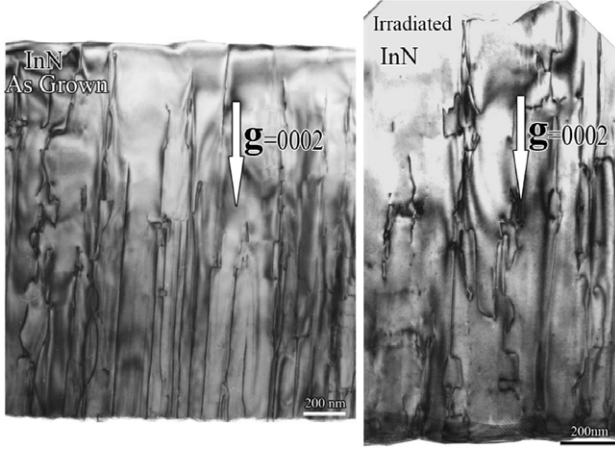


**Figure 15.** Cross sectional TEM micrographs of InN before (left,  $n = 1.6 \times 10^{18} \text{ cm}^{-3}$ ) and after (right,  $n = 4 \times 10^{20} \text{ cm}^{-3}$ ) irradiation with 2 MeV  $\text{He}^+$  ions at a dose of  $2.7 \times 10^{16} \text{ cm}^{-2}$ . The extended defect structure is not significantly affected by the radiation.

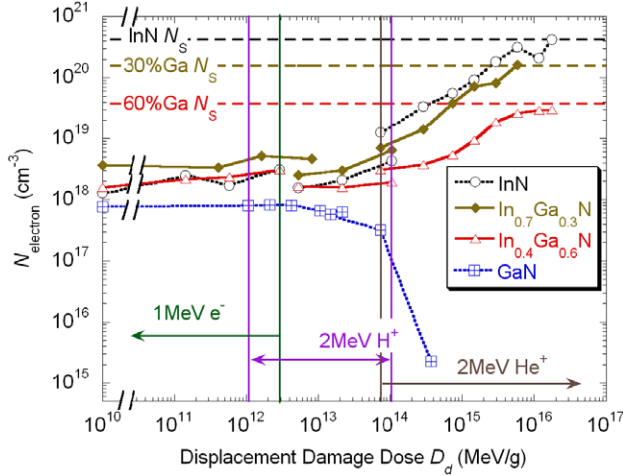


**Figure 16.** Free electron concentration in  $\text{In}_x\text{Ga}_{1-x}\text{N}$  as a function of displacement damage dose. The ranges of damage by different particles (electron, proton and  $^4\text{He}^+$ ) are labelled and the calculated saturation concentrations  $N_s$  for InN and  $\text{In}_{0.4}\text{Ga}_{0.6}\text{N}$  are also marked.

all measurements are performed on the same samples with progressively higher doses. Figure 16 shows the free electron concentration in four  $\text{In}_x\text{Ga}_{1-x}\text{N}$  samples, measured by room temperature Hall effect, as a function of  $D_d$ . The electron concentrations in InN and  $\text{In}_{0.4}\text{Ga}_{0.6}\text{N}$  increase with irradiation dose and then saturate at a maximum value at for  $D_d > 10^{16} \text{ MeV g}^{-1}$ . In contrast to In-rich InGaN, the electron concentration in GaN decreases with irradiation dose and the sample eventually becomes semi-insulating.

The opposite responses to irradiation damage between  $\text{In}_x\text{Ga}_{1-x}\text{N}$  and GaN can be attributed to the relative position of their band edges to  $E_{FS}$ . The band offset of  $\text{In}_x\text{Ga}_{1-x}\text{N}$  is plotted together with  $E_{FS}$  in the inset of figure 17. In  $\text{In}_x\text{Ga}_{1-x}\text{N}$  with  $x > 0.34$ , the conduction band edge is below  $E_{FS}$ . Thus, the irradiation-induced defects are predominantly donor-like (unless an  $\text{In}_x\text{Ga}_{1-x}\text{N}$  sample is heavily n-type to begin with) and raise the electron concentration. Once the

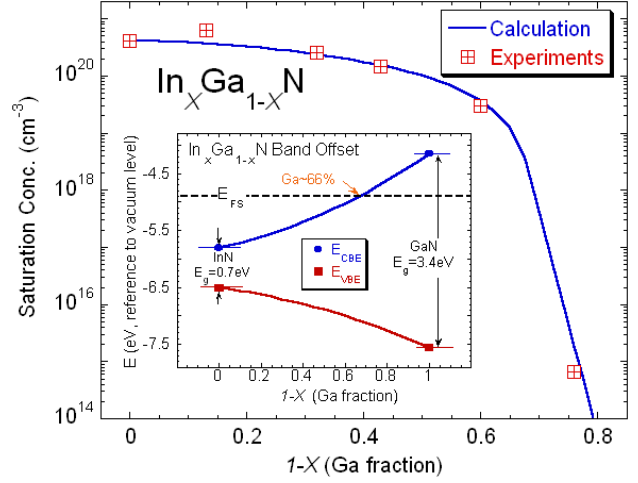


**Figure 17.** Electron saturation concentration of  $\text{In}_x\text{Ga}_{1-x}\text{N}$  as a function of Ga fraction. Square data points are measurements of the irradiation experiment and the solid line is the calculation result. Inset: the band offset diagram of  $\text{In}_x\text{Ga}_{1-x}\text{N}$  is shown with  $E_{FS}$ .

electron concentration is high enough that  $E_F$  reaches  $E_{FS}$ ,  $E_F$  is pinned as the formation rate of donor-like and acceptor-like defects becomes equal. On the other hand, in GaN (or  $\text{In}_x\text{Ga}_{1-x}\text{N}$  with  $x < 0.34$ ),  $E_{FS}$  is inside the bandgap, and therefore in n-type GaN, irradiation-induced defects are primarily acceptor-like and lower the electron concentration. The saturation concentration ( $N_s$ ) of  $\text{In}_x\text{Ga}_{1-x}\text{N}$  in heavily irradiated samples can be calculated by setting the Fermi level at  $E_{FS}$ :

$$N_s = \frac{1}{3\pi^2} \left( \frac{2m^*}{\hbar^2} \right)^{3/2} \times \int_{E_C}^{\infty} \frac{e^{((E-E_{FS})/k_B T)} [E - E_C + (E - E_C)^2 / E_g]^{3/2}}{[1 + e^{((E-E_{FS})/k_B T)}]^2} dE, \quad (4.1)$$

where  $E_C$  is the conduction band edge and  $E_g$  is the bandgap of  $\text{In}_x\text{Ga}_{1-x}\text{N}$ . In figure 17 the calculated  $N_s$  (solid line) is plotted together with experimental measurements (squares) of  $\text{In}_x\text{Ga}_{1-x}\text{N}$ . The excellent agreement between calculation and the experimental results suggests that particle irradiation can be an effective and simple method to control the doping (electron concentration) in In-rich  $\text{In}_x\text{Ga}_{1-x}\text{N}$  via native point defects.

#### 4.3. Surface electron accumulation layer in InN

In semiconductors the Fermi level stabilization energy plays another important role. It defines the defect-induced Fermi level pinning energy on semiconductor surfaces due to the existence of dangling bonds. Again, in most semiconductors the surface Fermi energy is pinned in the band gap resulting in the formation of a subsurface depletion region. In InN, pinning of the surface Fermi energy at 0.9 eV above the conduction band edge leads to a large accumulation of electrons in a subsurface layer. The surface accumulation layer of electrons has been found to be resistant to chemical or physical surface treatments. Evidence for this accumulation layer comes from electrolyte-based capacitance voltage (CV) measurements [54, 57], high-resolution electron-energy-loss

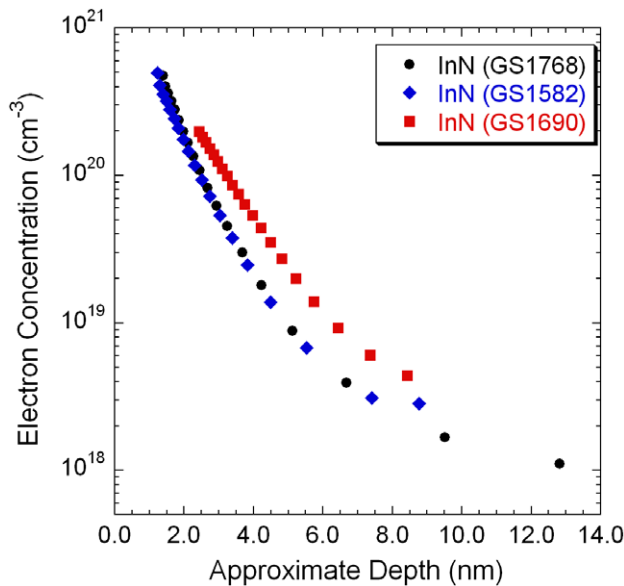


**Figure 18.** Electrolyte-based CV measurements of three nominally-undoped InN films showing electron concentration as a function of depth from the film surface.

spectroscopy (HREELS) [58] and studies of the dependence of the sheet electron concentration on film thickness, which showed that the sheet concentration had a linear slope with thickness but a non-zero intercept of  $(2.5\text{--}4.3) \times 10^{13} \text{ cm}^{-3}$  at zero thickness [57]. Figure 18 shows the accumulation of electrons at the surface as a function of depth obtained by CV measurements of typical InN films. The electron concentration has a maximum near the surface that rapidly decreases farther into the film, appearing to saturate at a value close to the bulk electron concentration measured by the Hall effect.

Calculations of the band bending at the surface that causes this electron accumulation layer provide further evidence of the applicability of the ADM. Mahboob *et al* [58] reported that at the surface of InN,  $E_F$  is pinned  $1.64 \pm 0.10 \text{ eV}$  above the valence band maximum, which is approximately the same position as  $E_{FS}$ . Indeed, if  $E_F$  were not pinned at  $E_{FS}$ , it would be expected that the surface charge accumulation could be altered by surface treatments that introduced additional native defects. This has not been found experimentally.

#### 4.4. Optical properties of irradiated InN and InGaN

We have used ‘defect doping’ to systematically study the effects of electron concentration on optical and electrical properties of InN and  $\text{In}_{1-x}\text{Ga}_x\text{N}$  alloys. As discussed below, this method provides more precise and reliable control over  $n$  than conventional doping methods in InN. Figure 19 shows the electron concentration as a function of 2 MeV  $\text{He}^+$  dose in four nominally-undoped InN samples. The increase in concentration is approximately linear with dose, and we find that the rate of electron generation is roughly 40 000 electrons/( $\text{He}^+ \text{ cm}$ ). In addition, the calculated  $N_S \sim 4 \times 10^{20} \text{ cm}^{-3}$  [54] is in good agreement with experiment. The results in figures 16 and 19 demonstrate that energetic particle irradiation is a method of predictable control of electron concentration in InN [54,59].

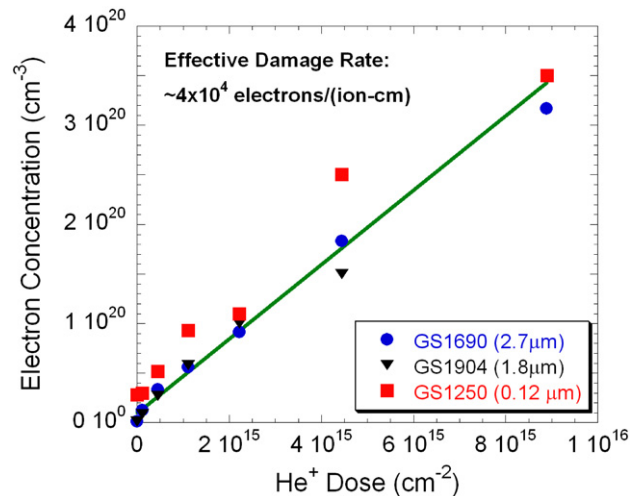


**Figure 19.** Electron concentration  $n$  as a function of 2 MeV  $\text{He}^+$  dose for three nominally-undoped InN films of varying thicknesses. The increase in  $n$  is linear in the dose and is consistent with a donor point defect production rate of  $4 \times 10^4 \text{ ion}^{-1} \text{ cm}^{-1}$ .

This type of ‘defect doping’ has several advantages over the conventional impurity doping. Since it is performed at room temperature it avoids any dopant segregation effects and gives a uniform donor defect distribution. Also, by varying the irradiation dose, different electron concentrations can be realized in the same starting material. This eliminates potential uncertainties associated with the variations in the crystal growth conditions that are required to achieve a range of impurity incorporation levels. It is evident from figure 16 that the defect doping can also be used to control the electron concentration in In-rich  $\text{In}_{1-x}\text{Ga}_x\text{N}$  alloys. However the doping concentration range decreases with increasing Ga content and is negligibly small when  $E_{FS}$  approaches the conduction band edge at  $x \sim 0.66$ .

We have used the defect doping to systematically study the Burstein–Moss shift in the absorption edge in InN and  $\text{In}_{1-x}\text{Ga}_x\text{N}$  alloys [60]. Figure 20(a) shows the evolution of the absorption spectrum of an InN sample with increasing  $\text{He}^+$  irradiation dose. Initially, the absorption edge shifts to a higher energy as irradiation dose increases, but eventually the shift saturates at a high dose. This is consistent with the increase of electron concentration and the saturation shown in figure 19. The observed large blue shift of the absorption edge is a clear manifestation of the Burstein–Moss shift described previously in section 2. As shown in figure 14, the shift of the absorption in the defect-doped InN is in a reasonably good agreement with the theoretical calculations and with results obtained from unintentionally doped samples. On the contrary, as shown in figure 20(b) the absorption edge of GaN does not change significantly as a result of the irradiation. Instead, an absorption feature appears at  $\sim 2.7 \text{ eV}$  and the intensity and line width increases with increasing irradiation dose. The energy position of this feature matches perfectly with the expected position of  $E_{FS}$  inside the GaN bandgap, indicating that empty or partially-filled defect states are created at the position of  $E_{FS}$  after irradiation.

The Burstein–Moss shift of the absorption spectra can be analysed numerically with equation (3.3) by varying the



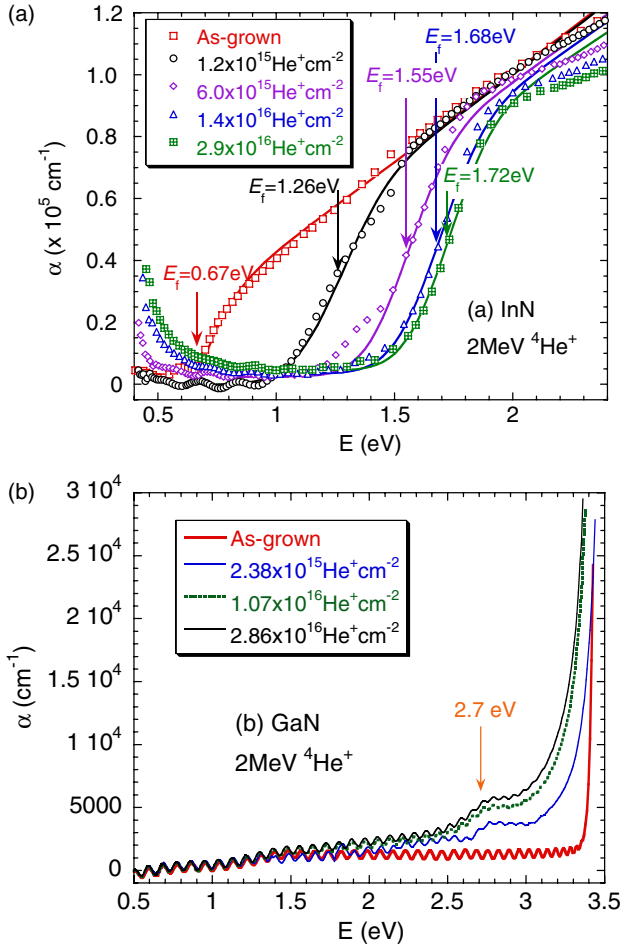


**Figure 20.** (a) The evolution of the absorption spectrum of InN with increasing  $^4\text{He}^+$  irradiation dose. The experiment results are shown as points and the calculation as lines. Fermi energies of the spectra from the fitting are labelled. (b) The evolution of the absorption of GaN with irradiation (experimental).

Fermi energy. To account for the broadening effects, a Gaussian function was convoluted with the energy-dependent absorption coefficient for a direct band gap:

$$\alpha(E) = \frac{1}{\Delta\sqrt{\pi}} \int_{-\infty}^{\infty} \alpha_0(E') \left[ 1 + \exp\left(\frac{E_F - E'}{k_B T}\right) \right]^{-1} \times \exp\left[-\left(\frac{E' - E}{\Delta}\right)^2\right] dE', \quad (4.2)$$

where  $\Delta$  is the Gaussian broadening parameter,  $\alpha_0$  is the absorption coefficient obtained from equation (3.3) and  $E_F$  is the Fermi energy. Equation (4.2) was used to fit the absorption data in figure 20(a) and excellent quantitative agreement was obtained. The resulting  $\Delta$  values from the best fits consistently lie between 0.21–0.23 eV, and the Fermi energy shifts from 0.67 eV in the as-grown sample to 1.72 eV after the heaviest dose of irradiation. The Fermi energies are in good agreement with those derived from the electron concentrations measured by the Hall effect.

The absorption edge at 1.72 eV observed in the samples exposed to the heaviest irradiation dose provides an insight into a recent report of a 1.7 eV bandgap for InN measured by valence electron energy loss spectroscopy (VEELS) [61].

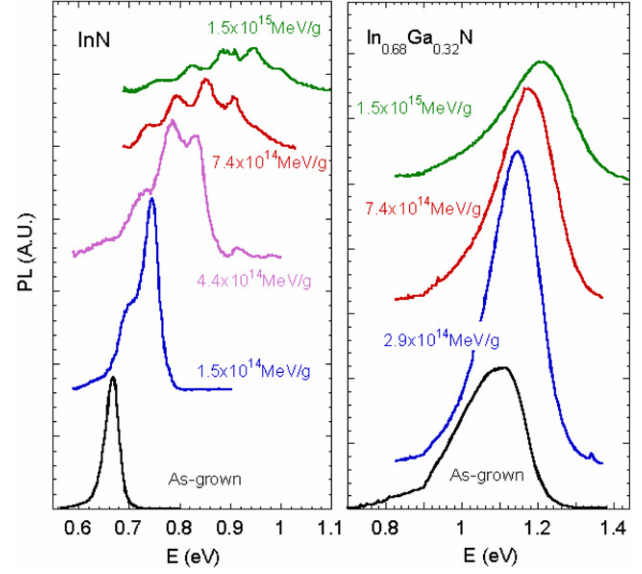


**Figure 21.** Evolution of PL spectra of InN and  $\text{In}_{0.68}\text{Ga}_{0.32}\text{N}$  upon increasing the dose of  $^4\text{He}^+$  irradiation. The PL measurements are performed on the same samples with increasing irradiation doses and the spectra are vertically offset.

These measurements involve focusing a 200 keV electron beam onto an area of about  $1 \text{ nm}^2$ . It should be noted that this electron energy is higher than the 80 keV threshold for displacement of the N atoms [62]. For typical VEELS experimental conditions (one second pulse at a beam current of 10 pA), the sample is irradiated with an electron dose of  $6 \times 10^{21} \text{ cm}^{-2}$ . Adopting the N site defect production rate of  $1 \text{ cm}^{-1}$  determined for GaN [62] we find that the concentration of defects produced in a VEELS experiment is more than an order of magnitude larger than the concentration required to stabilize the Fermi energy at  $E_{FS}$  in InN and to shift the optical absorption edge to 1.7 eV. It is therefore very likely that in VEELS experiments, damage-induced occupation of the conduction band states eliminates electronic transitions with energies smaller than 1.7 eV, giving an appearance of the band gap at this energy (i.e. the edge observed at 1.7 eV is a manifestation of the Burstein–Moss shift of the threshold for the inelastic electron scattering process).

The systematic study of the optical properties of the defect-doped InN has also been used to clarify a common misconception about the B–M shift. It has been argued that the B–M concept does not apply to InN because the blue shift of the PL emission does not follow the blue shift of the absorption edge [25, 63]. In fact, consideration of the nature of the optical transitions for the two cases, from occupied states in the valence band to empty states in the conduction band for absorption, and from occupied states in the conduction band to empty states in the valence band for PL, reveals that no B–M shift is expected for the PL. This is illustrated by comparing the effect of increasing the electron concentration on the absorption (figure 20) and PL (figure 21) spectra of InN and InGaN. A high irradiation dose shifts the absorption edge in InN by almost 1 eV (figure 20), whereas the PL peak energy shifts only by about 0.3 eV (figure 21). The shift and the broadening of the PL spectra shown in figure 21 can be understood by a breakdown of the momentum

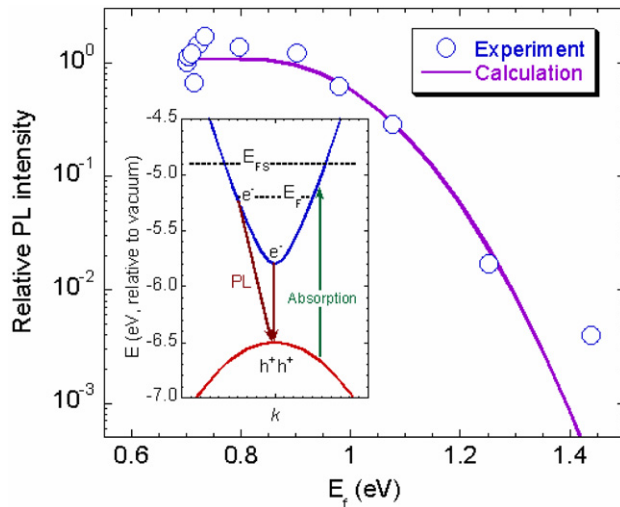


**Figure 22.** The relative PL intensity of InN from experiments (○) and calculations (—). Inset: a diagram showing the effect of momentum conservation breakdown on the observed PL spectrum.

conservation selection rule for optical transitions in heavily-doped samples [64]. The inset in figure 22 illustrates how the relaxation of the momentum conservation rule allows for optical transitions from all the occupied conduction band states to the top of the valence band, producing a blue-shifted and broadened PL spectrum. Thus, it is quite clear that blue shift of the PL line is expected to be always smaller than the absorption edge shift.

An unexpected feature of the PL spectra shown in figure 21 is that the rapid quenching of the PL intensity at very high irradiation doses is preceded by a slight increase in the PL intensity at low doses. It is well established that defect levels near the mid-gap are the most effective non-radiative recombination centres [65–67]. In In-rich  $\text{In}_x\text{Ga}_{1-x}\text{N}$  ( $x > 0.34$ ), the irradiation-induced defect levels lie above the conduction band and thus they are not effective non-radiative recombination centres. Instead, these donor-like defects raise the electron concentration, and the PL intensity increases as more carriers are available for recombination. However, as the irradiation dose and electron concentration increase,  $E_F$  approaches  $E_{FS}$ , resulting in an increased concentration of electrons trapped by defects. These electrons recombine non-radiatively with the valence band holes, quenching the luminescence at high irradiation doses. In figure 22, the relative PL intensity (circles) of an InN sample is plotted as a function of  $E_F$ . The solid line represents results of calculations assuming that the PL intensity is proportional to the majority carrier (electron) concentration and the minority carrier (hole) lifetime [68]. An inhomogeneous broadening resulting from the spatial variations of the Fermi energy to account for the diffuse nature of the PL quenching curve has been included in the calculations. As seen in figure 22, the calculations provide a good qualitative description of the experimental results.

#### 4.5. Electron concentration and mobility in InN

The electron concentrations and mobilities in as-grown InN samples vary widely. This can, in part, be attributed to the

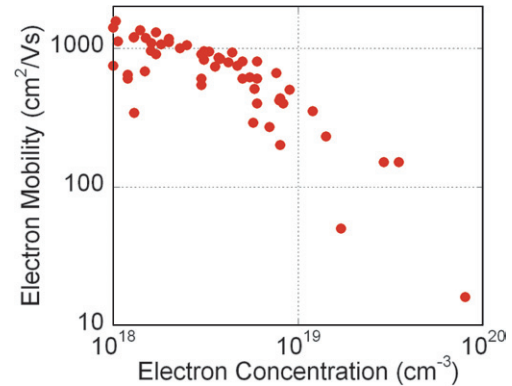


**Figure 23.** Electron mobility plotted versus electron concentration in as-grown InN films.

differing growth conditions. However, substantial variations of the electrical properties are also encountered in the films grown under similar conditions. For example, figure 23 shows a plot of electron mobility versus concentration for a number of InN films grown in the same MBE chamber. Notably, a considerable spread of the mobility values is observed in samples with the same electron concentration. In many instances the variations in electrical properties of InN samples can be traced to the surface electron accumulation effects discussed in section 4.3. To properly analyse the electron transport properties of InN and In-rich InGa<sub>N</sub> alloys, it is necessary to account for the contribution to the electrical conductivity from these electron accumulation layers at the surface and the interface. The importance of this conductance has been demonstrated by measuring the Hall effect in samples with varying thickness [69]. The surface electron density has been found to be  $(2\text{--}3) \times 10^{13} \text{ cm}^{-2}$  and has an electron mobility of  $\text{ca } 100 \text{ cm}^2 (\text{Vs})^{-1}$  [70]. The failure to realize the importance of the conductance of this layer to the total conductance can lead to errors in interpretation of the electrical properties of thin samples. A proper determination of the bulk electrical properties requires thick enough samples such that the contribution of surface conductivity can be neglected. This is especially important for samples with low bulk electron concentrations; in these cases, a layer thickness of at least  $1 \mu\text{m}$  is required to accurately determine the bulk properties.

In order to elucidate the transport properties of InN we have investigated samples irradiated with high energy particles to produce electron concentrations from  $10^{18}$  to up to mid- $10^{20} \text{ cm}^{-3}$ . The electron mobility as a function of electron concentration for samples made in this way is shown in figure 24. A striking feature of these results is the high level of reproducibility; the samples irradiated with the same dose have very similar electron concentrations and mobilities (as compared with the variations seen in figure 23 for as-grown films). This result confirms again that the process of defect formation via irradiation is determined by the intrinsic properties of InN rather than the properties of a specific sample.

In a first approach to understanding the mobility data presented in figure 24, the component electron mobilities associated with different scattering mechanisms were calculated assuming a simple parabolic band with the electron effective mass of  $0.07m_0$ . As seen in the figure, scattering by phonons (dashed lines) has a negligible

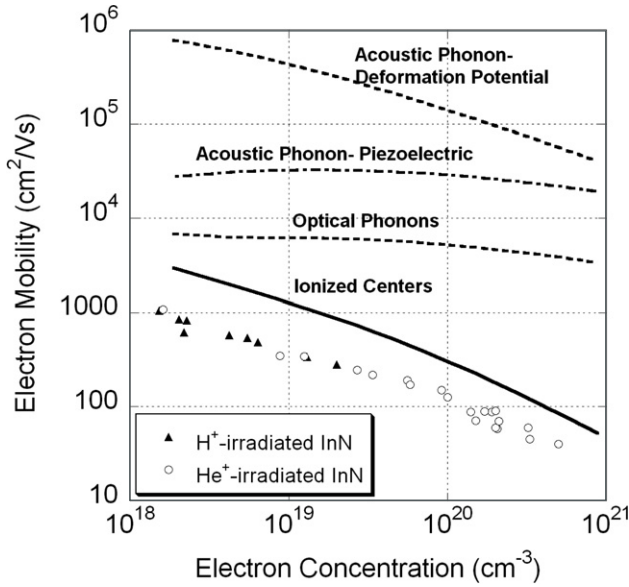


**Figure 24.** Electron mobility as a function of electron concentration in InN films irradiated with 2 MeV  $H^+$  and  $He^+$  ions. Contributions to the electron mobility from phonon-scattering mechanisms and ionized centre scattering are indicated by lines. Ionized impurity scattering is clearly the dominant mechanism; however, the theoretical mobilities obtained by assuming singly charged donors and no compensation are approximately three times larger than the experimental values (see text).

contribution to the mobility and can be safely ignored for the studied range of electron concentrations. The mobility limited by ionized impurity scattering was calculated assuming no compensation and singly-charged donor defects. The mobility limit obtained in this way is in agreement with the slope of the experimentally-observed concentration dependence of the electron mobility; however, the theoretical mobilities are over three times larger than the experimental values.

To analyse the electron mobility in greater detail we have carried out calculations of the electron scattering by multiply-charged defects in a non-parabolic conduction band. A constant, concentration-independent compensation ratio was also considered. We have adopted the model developed for narrow band gap semiconductors whose conduction is well described by the dispersion relation in equation (3.2). The electron mobility limited by ionized-impurity scattering is given by [70]:

$$\mu_i(k) = \frac{\varepsilon_0^2}{2\pi e^3 \hbar Z^2 N_i F_i} \left( \frac{dE}{dk} \right)^2 k, \quad (4.3)$$

where  $\varepsilon_0$  is the static dielectric constant (10.5 for InN [47]),  $Z$  is the charge of the ionized (defect) scattering centres,  $N_i$  is the concentration of scattering centres and  $F_i$  is a factor function that takes into account free electron screening effects as well as the reduction of the scattering rates resulting from the mixed nature of the conduction band wave functions [71]. This energy-dependent mobility is averaged with the Fermi-Dirac distribution function over the entire conduction band to give the macroscopic mobility as a function of electron concentration. Assuming that the ionized defects are triply-charged, uncompensated donors give a good fit to the data, as shown in figure 25.

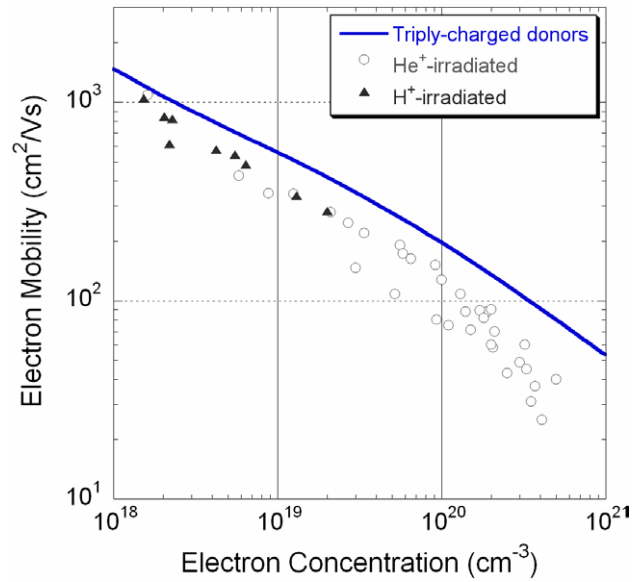


**Figure 25.** Calculations of electron mobility limited electron scattering by multiple charged defects in a nonparabolic conduction band in InN. The line shown was obtained for triply-charged donor defects and zero compensation and is in good agreement with experimental data.

#### 4.6. P-type doping of InN

P-type InN is essential to the realization of most of the desired applications of InN; however, fabrication of p-type material has proved to be very difficult, due to the propensity of InN for n-type conductivity. Only very recently has p-type InN using Mg acceptors been demonstrated [72], yet electrical contact to the material is still prevented by the n-type accumulation (inversion) layer that exists at the surface and isolates the p-type bulk. The evidence of p-type bulk material in Mg-doped InN films is reviewed below. To date p-type doping has not been achieved with any other acceptor.

We have studied InN samples intentionally doped with Mg. Secondary ion mass spectroscopy measurements indicate the total Mg concentration was between  $2 \times 10^{20}$  and  $2 \times 10^{21} \text{ cm}^{-3}$ . Electrolyte-based CV measurements of Mg-doped and undoped InN are shown in figure 26. The undoped sample shows the typical charge distribution: electron accumulation at the surface and constant charge in the bulk. In contrast, in Mg-doped InN the electron layer on the surface is followed by a p-type region that is observed as a change in the slope of the  $1/C^2$  dependence on the external bias. An analysis of the data in figure 26 leads to an estimate of the bulk concentration of acceptors on the order of  $10^{19} \text{ cm}^{-3}$ , which suggests that only a small fraction of the Mg atoms act as acceptors. A similar type of conversion from inversion n-type layer to the p-type bulk was observed in CV measurements of all Mg-doped InN samples.

The Hall effect measurements of InN:Mg show an n-type conduction with sheet electron concentrations between  $5 \times 10^{13}$  and  $7 \times 10^{14} \text{ cm}^{-2}$  and with electron mobilities ranging from 15 to  $90 \text{ cm}^2 (\text{Vs})^{-1}$ . If the Mg-doped films were assumed to be n-type throughout the bulk, the electron concentrations would become  $1 \times 10^{18}$ – $1 \times 10^{19} \text{ cm}^{-3}$  and the corresponding mobility values would then be one order of magnitude lower

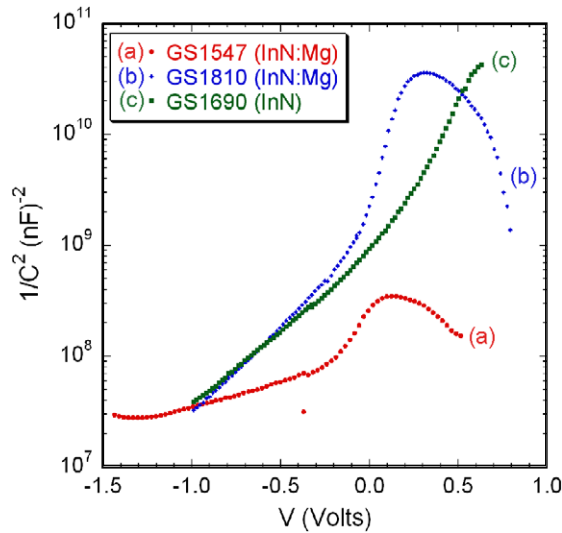


**Figure 26.** CV data for undoped and Mg-doped InN obtained using an electrolyte surface contact. The change in the slope observed for the two Mg-doped samples as the voltage increases is indicative of a type change as the depletion region extends past the n-type surface inversion layer.

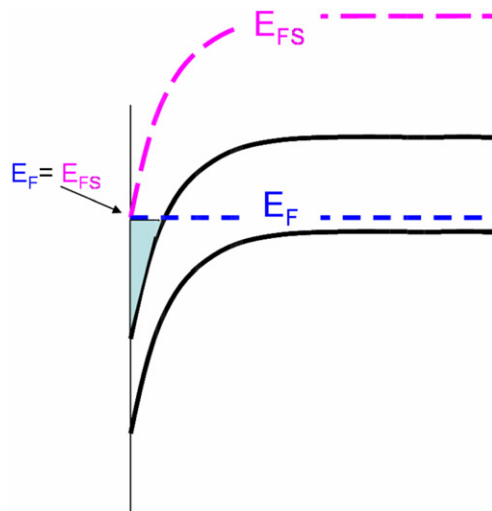


**Figure 27.** Schematic of the band structure of Mg-doped InN, showing the electron inversion layer (shaded). The Fermi energy ( $E_F$ ) and the Fermi level stabilization energy ( $E_{FS}$ ), which pins  $E_F$  at the surface, are also shown. The low electron mobility values in Mg-doped InN can be understood assuming that Hall effect measurements only evaluate properties of the n-type surface inversion layer, which is electrically isolated from the p-type bulk. The low electron mobility is consistent with an average surface electron density of low  $10^{20} \text{ cm}^{-3}$  in the inversion layer.

than those found in undoped, n-type InN films. As shown schematically in figure 27, the low electron mobility values in Mg-doped InN can be understood assuming that Hall effect measurements only evaluate properties of the n-type surface inversion layer, which are electrically isolated from the p-type bulk. The low electron mobility is consistent with an average surface electron density of the low  $10^{20} \text{ cm}^{-3}$  in the inversion layer.

Donor defect doping by high-energy particle irradiation can be used to achieve precisely-controlled type conversion of

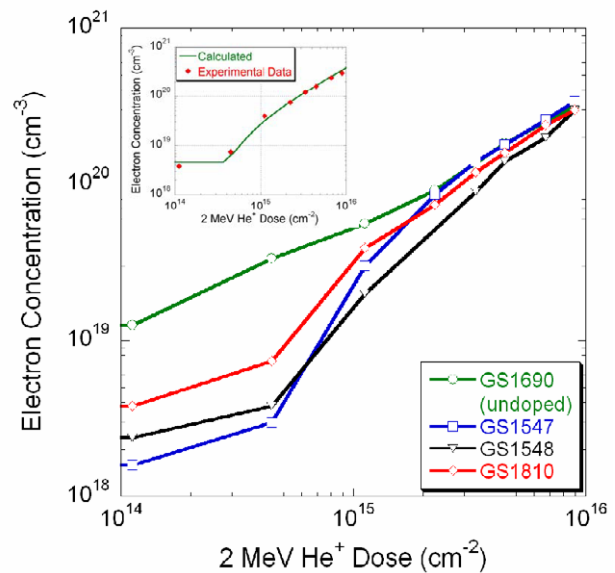


**Figure 28.** Electron concentration as a function of 2 MeV  $\text{He}^+$  dose in three Mg-doped InN films and one undoped film. It should be noted that the electron concentration is obtained from Hall effect measurements assuming a uniform film. Inset: calculations of electron concentration plotted with the experimental data for one Mg-doped film (GS1810).

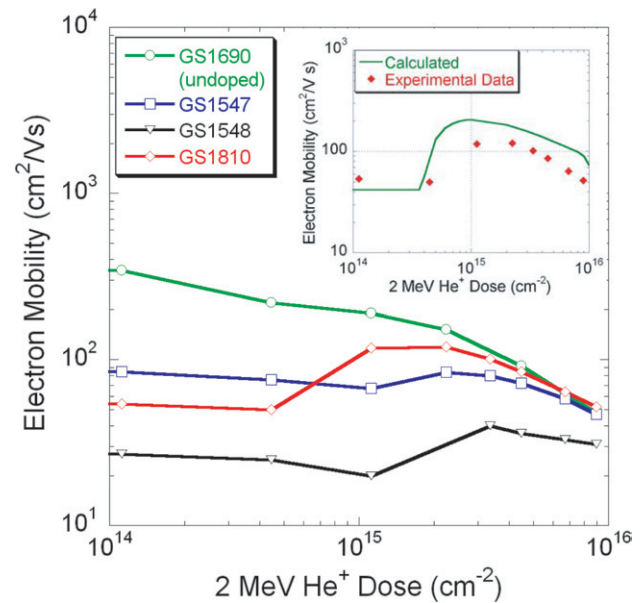


**Figure 29.** Electron mobility as a function of 2 MeV  $\text{He}^+$  dose in three Mg-doped InN films and one undoped film. As in figure 28, the mobility values are obtained from Hall effect measurements assuming uniform films. Inset: calculations of electron mobility plotted with the experimental data for one Mg-doped film.

the bulk Mg-doped, p-type layer. Figures 28 and 29 show the electron concentration and electron mobility, respectively, in Mg-doped films and, for comparison, in one unintentionally doped n-type film. At low doses of  $\text{He}^+$  irradiation, the electron concentration and mobility in Mg-doped films is approximately constant, as only the n-type surface inversion layer is measured. After irradiation doses close to  $10^{15} \text{ cm}^{-2}$ ,



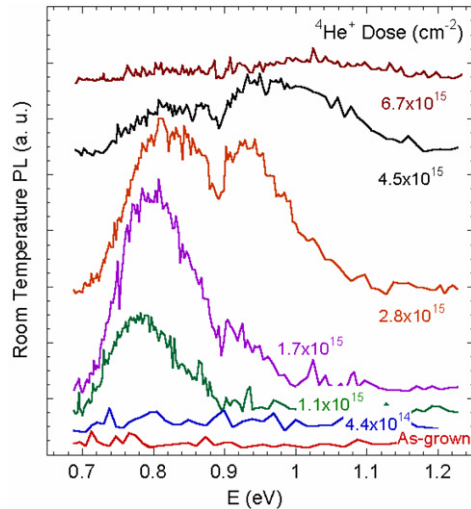


**Figure 30.** PL spectra of one Mg-doped film (GS1810) as a function of the 2 MeV  $\text{He}^+$  dose, showing the onset of PL after a dose of  $1.1 \times 10^{15} \text{ cm}^{-2}$ , followed by its quenching after a dose of  $6.7 \times 10^{15} \text{ cm}^{-2}$ .

i.e. doses which introduce electron concentrations in the low- $10^{19} \text{ cm}^{-3}$  and are sufficient to overcompensate the p-type bulk, the Mg-doped films show increases in electron concentration and mobility that converge upon higher doses to the values of the undoped film. This behaviour is in sharp contrast to that of irradiated, undoped films, but it can be satisfactorily modelled using the assumption of a p-type bulk layer and an n-type surface inversion layer. The insets exhibit the comparison of the model calculations with the experimental data in the InN:Mg sample with the lowest Mg content. As is seen in figures 28 and 29, the modelling provides a good qualitative description of the experimental results.

One of striking effects of Mg doping is that PL has not been observed in as-grown, Mg-doped InN films, while nearly all single crystal, undoped films show strong band edge PL signal. As shown in figure 27, a possible reason for this could be a large subsurface electric field that separates the free electrons from holes in Mg-doped samples. The field can be reduced by compensating the bulk p-type layer, and therefore it is expected that the band edge emission could be restored by the donor defect doping through a high energy particle irradiation. Figure 30 shows the evolution of the PL signal in InN:Mg as a function of the irradiation dose in the sample with the lowest Mg content. A PL signal was observed after a 2 MeV  $\text{He}^+$  dose of  $1.1 \times 10^{15} \text{ cm}^{-2}$ , and it persisted until quenching at a dose of  $6.7 \times 10^{15} \text{ cm}^{-2}$ . Comparison of the results in figures 28–30 shows that the PL onset occurs at a dose of  $1.1 \times 10^{15} \text{ cm}^{-2}$ , which is approximately twice the dose that compensates the Mg acceptors and begins to create an n-type conductivity in the bulk of the film. This is additional proof that highly-irradiated Mg-doped films behave as undoped, n-type InN films once the initially-p-type bulk layer is converted to n-type.

## 5. Summary and outlook

The availability of high quality, MBE-grown InN and In-rich InGaN films has allowed the fundamental properties of InN to be re-evaluated. Use of optical methods (absorption, PL,

and PR), complemented with soft x-ray measurements and the detailed study of the bowing parameter in InGaN, agree on a fundamental band gap of InN of  $6.65 \pm 0.05 \text{ eV}$  instead of the previously accepted value of 1.9 eV. The small band gap exhibits weaker temperature and pressure dependences than those of GaN and AlN. The strong  $k \cdot p$  interaction across the narrow gap leads to a highly non-parabolic conduction band. The free electron effective mass ranges from  $0.07m_0$  at the bottom of the conduction band to  $0.26m_0$  in InN with an electron concentration,  $n$ , of  $7 \times 10^{20} \text{ cm}^{-3}$ . Occupation of the conduction band at high values of  $n$  causes a Burstein–Moss shift from 0.7 to 1.7 eV. This effect provides an explanation for the wide range of InN band gaps reported previously.

The generation of donor-like point defects by energetic particle irradiation (using electrons,  $\text{H}^+$  and  $\text{He}^+$  ions) is shown to be an effective method for controlling the electron concentration in nominally-undoped InN. Furthermore, this allows fundamental studies of the energy levels of native defects in InN and of electron transport. Optical measurements of the Burstein–Moss shift of the absorption edge, Hall effect measurements and PL are used to show that native point defects in InN have an energy level (the Fermi stabilization energy,  $E_{\text{FS}}$ )  $1.64 \pm 0.10 \text{ eV}$  above the valence band edge. The location of  $E_{\text{FS}}$  in the conduction band of InN is responsible for the n-type activity of nearly all InN synthesized to date. In addition, InN has a surface accumulation layer of electrons which is consistent with Fermi level pinning at  $E_{\text{FS}}$ . The saturation electron concentration of  $4 \times 10^{20} \text{ cm}^{-3}$  is achieved when the Fermi level in the bulk reaches  $E_{\text{FS}}$ . Scattering by triply-charged donors is shown to be the predominant electron scattering mechanism in InN at room temperature.

Experimental evidence for p-type activity in InN doped with Mg is evaluated. The surface inversion layer of electron precludes the possibility of direct electrical contact to p-type material below the surface. Electrolyte-based CV measurements, Hall effect and PL measurements of as-grown and irradiated InN:Mg films are modelled assuming an n-type surface layer and a p-type bulk.

## Acknowledgments

The work at LBNL was supported by the Director's Innovation Initiative Program, National Reconnaissance Office and by the US Department of Energy, Office of Science, Office of Basic Energy Sciences, Division of Materials Science under Contract No DE-AC02-05CH11231. We thank H Lu and W J Schaff of Cornell University for providing MBE films and M Yeh of Blue Photonics for providing MOCVD films. R E Jones was supported by the Department of Defense through a National Defense Science and Engineering Graduate fellowship.

## References

- [1] Nakamura S, Pearton S and Fasol G 2000 *The Blue Laser Diode: The Complete Story* (Berlin: Springer)
- [2] Steranka F M *et al* 2002 *Phys. Status Solidi a* **194** 380
- [3] Hovel H J and Cuomo J J 1972 *Appl. Phys. Lett.* **20** 71
- [4] Tyagi V A, Eustignev V A, Krasilo A M, Andreeva A F and Malatidou V Yu 1977 *Sov. Phys. Semicond.* **11** 1257
- [5] Westra K I, Lawson R P W and Brett M J 1988 *J. Vac. Sci. Technol. A* **8** 1730

- [6] Tansley T L and Foley C P 1984 *Semi-Insulating III-V Compounds* ed D C Look and J S Blakemore (London: Shiva) p 497
- [7] Butcher K S A, Winterhert-Fouquet M, Chen P P T, Tansley T L and Srikeaw S 2001 *Mater. Res. Symp. Proc.* **693** 16.9
- [8] Tansley T L and Foley C P 1986 *J. Appl. Phys.* **59** 3241
- [9] Matsuoka T, Tanaka H and Katsui A 1990 *Int. Symp. on GaAs and Related Compounds (Karuizawa, 1989) (Ins. Phys. Conf. Series vol 106)* p 141
- [10] Yamaguchi S, Kariya M, Nitta S, Takeuchi T, Wetzel C, Amano H and Akasaki I 2000 *Appl. Phys. Lett.* **76** 876
- [11] Lu H, Schaff W J, Hwang J, Wu H, Yeo W, Pharkya A and Eastman L F 2000 *Appl. Phys. Lett.* **77** 2548  
Lu H, Schaff W J, Hwang J, Wu H, Koley G and Eastman L F 2001 *Appl. Phys. Lett.* **79** 1489–91
- [12] Davydov V Yu *et al* 2002 *Phys. Status Solidi b* **229** R1
- [13] Sugita K, Takatsuka H, Hashimoto A and Yamamoto A 2003 *Phys. Status Solidi b* **240** 421
- [14] Saito Y, Yamaguchi T, Kano K, Araki T, Nanishi Y, Teraguchi N and Suzuki A 2002 *J. Cryst. Growth* **237** 1017  
Saito Y, Harima H, Kurimoto E, Yamaguchi T, Teraguchi N, Suzuki A, Araki T and Nanishi Y 2002 *Phys. Status Solidi b* **234** 796
- [15] Swartz C H, Tomkins R P, Myers T H, Lu H and Schaff W J 2005 *Phys. Status Solidi c* **2** 2250
- [16] Wu J, Walukiewicz W, Yu K M, Ager J W III, Haller E E, Lu H, Schaff W J, Saito Y and Nanishi Y 2002 *Appl. Phys. Lett.* **80** 3967
- [17] Nanishi Y, Saito Y and Yamaguchi T 2003 *Japan. J. Appl. Phys.* **42** 2549
- [18] Bechstedt F, Furthmüller J, Ferhat M, Teles L K, Scolfaro L M R, Leite J R, Davydov V Yu, Ambacher O and Goldhahn R 2003 *Phys. Status Solidi a* **195** 628–33
- [19] Carrier P and Su-Huai Wei 2005 *J. Appl. Phys.* **97** 033707
- [20] Shubina T V *et al* 2004 *Phys. Rev. Lett.* **92** 117407
- [21] Butcher K S A, Winterhert-Fouquet M, Chen P P T, Tansley T L, Dou H, Shrestha S K, Timmers H, Kuball M, Prince K E and Bradby J E 2004 *J. Appl. Phys.* **95** 124
- [22] Wu J and Walukiewicz W 2003 *Superlatt. Microstruct.* **34** 63
- [23] Davydov V Yu and Klochikhin A A 2004 *Semiconductors* **38** 861
- [24] Monemar B, Paskova P P and Kasic A 2005 *Superlatt. Microstruct.* **38** 38
- [25] Butcher K S A and Tansley T L 2005 *Superlatt. Microstruct.* **38** 1
- [26] Goldhahn R *et al* 2004 *Superlatt. Microstruct.* **36** 591
- [27] Bhuiyan A G, Hashimoto A and Yamamoto A 2003 *J. Appl. Phys.* **94** 2776
- [28] Ho I-H and Stringfellow G B 1996 *Appl. Phys. Lett.* **69** 2701
- [29] Saito T and Arakawa Y 1999 *Phys. Rev. B* **60** 1701
- [30] Ferhat M and Bechstedt F 2002 *Phys. Rev. B* **65** 075213
- [31] Doppalapudi D, Basu S N, Ludwig K F and Moustakas T D 1998 *J. Appl. Phys.* **84** 1389
- [32] El-Masry N A, Piner E L, Liu S X and Bedair S M 1998 *Appl. Phys. Lett.* **72** 40
- [33] Wakahara A, Tokuda T, Dang X-D, Noda S and Sasaki A 1997 *Appl. Phys. Lett.* **71** 906
- [34] Rao M, Kim D and Mahajan S 2004 *Appl. Phys. Lett.* **85** 1961
- [35] Liliental-Weber Z, Zakharov D N, Yu K M, Ager J W III, Walukiewicz W, Haller E E, Lu H and Schaff W J 2005 *J. Electron Microsc.* **54** 243
- [36] Hernández S, Cuscó R, Pastor D, Artús L, O'Donnell K P, Martin R W, Watson I M, Nanishi Y and Calleja E 2005 *J. Appl. Phys.* **98** 013511
- [37] Yu K M, Liliental-Weber Z, Walukiewicz W, Li S X, Jones R E, Shan W, Ager J W III, Haller E E, Lu H and Schaff W J 2005 *Appl. Phys. Lett.* **86** 71910
- [38] Ager J W III, Liliental-Weber Z, Yu K M, Walukiewicz W, Zakharov D N, Haller E E, Lu H and Schaff W J 2006 *Appl. Phys. Lett.* submitted
- [39] Wu J, Walukiewicz W, Shan W, Yu K M, Ager J W III, Li S X, Haller E E, Lu H and Schaff W J 2003 *J. Appl. Phys.* **94** 4457
- [40] Wu J, Walukiewicz W, Yu K M, Shan W, Ager J W III, Haller E E, Lu H, Schaff W J, Metzger W K and Sarah Kurtz 2003 *J. Appl. Phys.* **94** 6477
- [41] Denlinger J D *et al* unpublished results
- [42] Wu J, Walukiewicz W, Shan W, Yu K M, Ager J W III, Li S X, Haller E E, Lu H and Schaff W J 2003 *Solid State Commun.* **127** 411 and references therein.
- [43] Wei S H, Nie X, Batyrev I G and Zhang S B 2003 *Phys. Rev. B* **67** 165209
- [44] Kane E O 1957 *J. Phys. Chem. Solids* **1** 249
- [45] Washburn H A, Sites J R and Wieder H H 1997 *J. Appl. Phys.* **50** 4872
- [46] Perlin P *et al* 1996 *Appl. Phys. Lett.* **68** 1114
- [47] Inushima T, Higashiwaki M and Matsui T 2003 *Phys. Rev. B* **68** 235204
- [48] Wu J, Walukiewicz W, Shan W, Yu K M, Ager J W III, Haller E E, Lu H and Schaff W J 2002 *Phys. Rev. B* **66** 201403 and references therein
- [49] Wu J *et al* 2004 *Appl. Phys. Lett.* **84** 2805
- [50] Kasic A, Valcheva E, Monemar B, Lu H and Schaff W J 2004 *Phys. Rev. B* **70** 115217
- [51] Lu H, Schaff W J, Eastman L, Wu J, Walukiewicz W, Look D C and Molnar R J 2002 *Mater. Res. Soc. Symp. Proc.* **743** L4.10.1
- [52] Walukiewicz W 1989 *Appl. Phys. Lett.* **54** 2094
- [53] Walukiewicz W 2001 *Physica B* **302** 123
- [54] Li S X, Yu K M, Wu J, Jones R E, Walukiewicz W, Ager J W III, Shan W, Haller E E, Lu H and Schaff W J 2005 *Phys. Rev. B* **71** 161201
- [55] Messenger S R, Summers G P, Burke E A, Walters R J and Xapsos M A 2001 *Prog. Photovoltaics: Res. Appl.* **9** 103
- [56] Messenger S R, Burke E A, Summers G P, Xapsos M A, Walters R J, Jackson E M and Weaver B D 1999 *IEEE Trans. Nucl. Sci.* **46** 1595
- [57] Lu H, Schaff W J, Eastman L, Stutz C E 2003 *Appl. Phys. Lett.* **82** 1736
- [58] Mahboob I, Veal T D, McConville C V, Lu H and Schaff W J 2004 *Phys. Rev. Lett.* **92** 036804
- [59] Jones R E, Li S X, Hsu L, Yu K M, Walukiewicz W, Liliental-Weber Z, Ager J W III, Haller E E, Lu H and Schaff W J 2006 *Physica B* submitted
- [60] Li S X, Haller E E, Yu K M, Walukiewicz W, Ager J W III, Wu J, Shan W, Hai Lu and William J Schaff 2005 *Appl. Phys. Lett.* **87** 161905
- [61] Specht P, Ho J C, Xu X, Armitage R, Weber E R, Erni R and Kisielowski C 2005 *Solid State Commun.* **135** 340
- [62] Look D C, Reynolds D C, Hemsky J W, Sizemore J R, Jones R L and Molnar R J 1997 *Phys. Rev. Lett.* **79** 2273
- [63] Ho J C, Specht P, Yang Q, Xu X, Hao D and Weber E R 2005 *J. Appl. Phys.* **98** 093712
- [64] Arnaudov B, Paskova T, Paskov P P, Magnusson B, Valcheva E, Monemar B, Lu H, Schaff W J, Amano H and Akasaki I 2004 *Phys. Rev. B* **69** 115216
- [65] Langer J M and Walukiewicz W 1995 *Mater. Sci. Forum* **196–201** 1389
- [66] Nolte D D 1990 *Solid-State Electron.* **33** 295
- [67] Aspnes D E 1983 *Surf. Sci.* **132** 406
- [68] Li S X *et al* unpublished
- [69] Swartz C H, Tompkins R P, Giles N C, Myers T H, Lu H, Schaff W J and Eastman L F 2004 *J. Cryst. Growth* **269** 29
- [70] Schaff W J, Lu H, Eastman L F, Walukiewicz W, Yu K M, Keller S, Kurtz S, Keyes B and Gevilas L 2004 *ECS Proc.* vol 2004–06, ed V-H Ng and A G Baca (Pennington NJ: Electrochemical Society) p 358
- [71] Zawadzki W and Szymanska W 1971 *Phys. Status Solidi b* **45** 415
- [72] Jones R E, Yu K M, Li S X, Walukiewicz W, Ager J W III, Haller E E, Lu H and Schaff W J 2006 submitted